catalysts

MDPI

*Article*

# Acid-Catalyzed One-Pot Synthesis of Unsymmetrical Monocarbonyl Curcuminoids: DFT Study, Molecular Docking and Molecular Dynamics Simulation of Their Tubulin-Targeting Potential

**Waqas Rafiq and Akbar Ali ***

Department of Chemistry, Government College University Faisalabad, Faisalabad 38000, Pakistan
* Correspondence: akbarali@gcuf.edu.pk

**Abstract**

This study focuses on the potential tubulin-targeting properties of four unsymmetrical monocarbonyl curcuminoids, particularly their interaction with the colchine-binding site. **CMND** ((1E,4E)-5-(2-chloro-4-methoxyphenyl)-2-methyl-1-(4-nitrophenyl)penta-1,4-dien-3-one), **CMNP** ((1*E*,4*E*)-5-(3-chloro-4-methoxyphenyl)-2-methyl-1-(4-nitrophenyl)penta-1,4-dien-3-one), **MMND** ((1*E*,4*E*)-5-(4-methoxy-3-methylphenyl)-2-methyl-1-(4-nitrophenyl)penta-1,4-dien-3-one), and **IMNP** ((1*E*,4*E*)-5-(4-iodophenyl)-2-methyl-1-(4-nitrophenyl) penta-1,4-dien-3-one) were synthesized *via* a one-pot acid-catalyzed, two-step aldol condensation, structurally characterized by $^{1}$H and $^{13}$C NMR and IR spectroscopy. Molecular docking against tubulin indicated that all four compounds occupy the colchicine-binding site, with binding energies of −8.38 to −9.04 kcal/mol. **IMNP** exhibited the most favorable docking energy (−9.04 kcal/mol), while conserved interactions involving Asn206 and Ala12 were observed across the complexes. However, 100 ns molecular dynamics (MD) simulations revealed differences in dynamic behavior among the complexes, with **CMNP** showing the most favorable dynamic stability. **CMNP** also showed the most favorable binding-free energy ($\Delta G_{bind}$ = −20.93 ± 4.77 kcal/mol) in MM-PBSA analysis, followed by **CMND**, **IMNP**, and **MMND**. Complementary density functional theory (DFT) calculations at the ωB97X-D/6-31+G(d,p) level indicated strong intramolecular-charge-transfer character across the conjugated dienone-aryl network. **MMND** possessed the smallest HOMO-LUMO gap (6.89 eV), suggesting comparatively high chemical reactivity within the series. Nonlinear optical (NLO) calculations further indicated pronounced polarizability and first hyperpolarizability. Overall, the docking and MD results highlights **CMNP** as a promising candidate for further evaluation as a potential tubulin-targeting agent, while the DFT and NLO calculations provide complementary insights into the electronic and optical properties of the synthesized compounds.

**Keywords:** unsymmetrical monocarbonyl curcuminoids; one-pot aldol condensation; molecular docking; molecular dynamics; DFT

Check for updates

Academic Editor: Vincenzo Patamia

Received: 22 October 2026
Revised: 19 November 2026
Accepted: 24 November 2026
Published: 27 November 2026

**Copyright:** © 2026 by the authors. Licensee MDPI, Basel, Switzerland. This article is an open access article distributed under the terms and conditions of the Creative Commons Attribution (CC BY) license.

## 1. Introduction

Cancer remains a major global health burden, with an estimated 20.6 million new cases and 9.8 million cancer-related deaths recorded worldwide in 2024, nearly half of which occurred in Asia [1]. Despite remarkable clinical success of chimeric antigen receptor T-cells

(CAR-T) in hematological malignancies, significant challenges persist, including treatment-associated toxicities such as cytokine release syndrome, limited efficacy in solid tumors due to poor T-cell infiltration and an immunosuppressive tumor microenvironment, and the emergence of therapeutic resistance [2]. These limitations continue to drive the search for novel molecular targets and anticancer agents with improved therapeutic potential.

Malignant cells depend on tightly regulated processes governing cell division for sustained proliferation, making proteins involved in mitosis attractive targets for anticancer drug development. Given the clinical success of diverse microtubule-targeting agents and their fundamental role in disrupting mitotic spindle formation and chromosome segregation, microtubules have been identified as the best cancer target [3]. Pharmacological disturbance of microtubule dynamics disrupts mitotic spindle function, resulting in cell-cycle arrest at the metaphase/anaphase transition and subsequent induction of apoptotic cell death [4]. The clinical success of diverse microtubule-targeting agents, including taxanes, vinca alkaloids, and colchicine-binding site inhibitors, demonstrates the therapeutic importance of tubulin-directed drug discovery and establishes microtubules as a premier anticancer target with broad spectrum activity [5].

Microtubules are dynamic cytoskeletal polymers assembled from α- and β-tubulin heterodimers that play fundamental roles in chromosome segregation, intracellular trafficking, cell morphology, and maintenance of cellular structure [6]. Their biological functions depend on a tightly regulated equilibrium between polymerization and depolymerization, with the dynamic character of microtubules being key to their cellular functions [7]. Small molecules that perturb this dynamic behavior can interfere with mitotic spindle formation and progression through mitosis, frequently resulting in cell-cycle arrest and subsequent cell death [8]. Microtubule-targeting agents, including vinca alkaloids and taxanes that have been used clinically for over 50 years, represent some of the most effective and clinically validated anticancer drugs available for treating solid tumors and hematological malignancies, despite their associated toxicities in normal proliferating tissues.

Several structurally characterized ligand-binding regions have been identified on tubulin, including the taxane, vinca, and colchicine-binding sites, providing distinct opportunities for pharmacological evaluation [9]. Among these, the colchicine-binding site has received considerable attention because of its structurally adaptable binding environment and capacity to accommodate chemically diverse small-molecule scaffolds [10]. Binding of small molecules within this region can induce conformational changes in tubulin and perturb microtubule assembly and dynamics, ultimately interfering with mitotic progression [11]. Selected colchicine-site inhibitors have demonstrated activity against drug-resistant cancer models, including paclitaxel-resistant prostate cancer and vincristine-resistant neuroblastoma xenografts [12]. However, the ability to overcome resistance is highly dependent on the chemical scaffold and underlying resistance mechanism, as demonstrated by structure–activity studies showing 10-fold potency differences between closely related compounds [13]. Consequently, the colchicine-binding site remains an attractive region for the discovery and optimization of novel tubulin-targeting anticancer compounds.

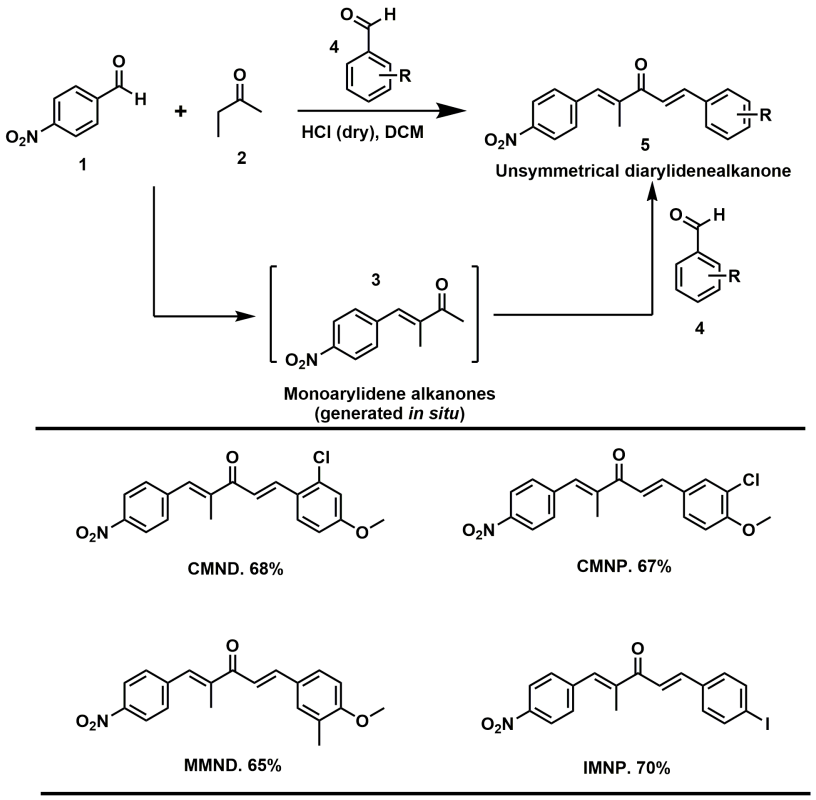
Curcumin, derived from Curcuma longa, demonstrates extensive pharmacological activities including anticancer, anti-inflammatory, antioxidant, and antimicrobial effects through modulation of multiple molecular targets including transcription factors, protein kinases, and inflammatory cytokines [14,15]. Recently, curcumin-derived polyphenolic building blocks have also been analyzed in advanced anticancer approaches, including mitochondria-targeted copper delivery to promote cuproptosis in order to tackle cisplatin resistance in cancer cells [16]. Beyond its biological potential, curcumin has been noticed for its characteristic physicochemical properties, such as light-absorbing and free-radical-scavenging abilities, which have recently been exploited in innovative ceramic 3D-printing

technologies [17]. Despite its therapeutic potential, curcumin's clinical application remains limited due to poor aqueous solubility, chemical instability, rapid hepatic metabolism, and consequently low systemic bioavailability when administered orally [18]. These limitations have motivated extensive efforts to develop structurally modified curcuminoids with improved physicochemical and pharmacological properties. Comparable molecular-tailoring approaches have also been analyzed for other natural-product-derived anticancer agents, where structural modification can improve their therapeutic potential [19].

Monocarbonyl curcuminoids represent an important class of curcumin derivatives where the unstable β-diketone moiety is replaced with a monocarbonyl bridge, resulting in greatly enhanced chemical stability and improved pharmacokinetic properties [20]. This structural modification preserves the extended conjugated framework and biological activity while enabling substantial structural diversification [21]. Numerous monocarbonyl curcuminoids have demonstrated promising antiproliferative activity against different cancer cell models [22,23]. Furthermore, structure–activity relationship studies indicate that aromatic substitution and electronic effects can substantially influence their molecular properties and biological activity, with aromatic ring modifications shown to adjust electronic properties, lipophilicity, and cellular entry [24]. In particular, electron-donating and electron-withdrawing substituents can modify electronic distribution, polarity, molecular conformation, and noncovalent interactions with biological targets.

The demonstrated interaction of curcumin and its derivatives with tubulin, along with their ability to inhibit microtubule assembly, provides a strong rationale for investigating these compounds as potential tubulin-targeting anticancer agents [25]. While curcumin has been shown to bind tubulin at a unique site distinct from the colchicine-binding region and structural modifications of curcuminoid derivatives significantly influence their tubulin-targeting activity, the molecular determinants governing these interactions remain incompletely understood [26]. The characterization of binding modes for newly synthesized unsymmetrical monocarbonyl curcuminoids represents a critical knowledge gap that limits the rational design of more potent tubulin-targeting agents within this promising scaffold class.

In the present study, newly synthesized unsymmetrical monocarbonyl curcuminoids were investigated through an integrated experimental and computational approach. The compounds were synthesized using a one-pot acid-catalyzed strategy and characterized by appropriate analytical and spectroscopic techniques (Scheme 1). DFT calculations were employed to characterize their electronic properties, while molecular docking against tubulin (PDB ID: 6O5M) was used to investigate their predicted binding modes and key protein–ligand interactions. Molecular dynamics simulations were subsequently performed for selected complexes to examine the stability and dynamic behavior of the predicted binding modes. Collectively, these analyses were used to establish structure–property–interaction relationships and identify promising structural features for further investigation of unsymmetrical monocarbonyl curcuminoids as potential tubulin-targeting anticancer leads.




**Scheme 1.** Acid-catalyzed synthesis of unsymmetrical monocarbonyl curcuminoids.

## 2. Results and Discussion

### *2.1. Molecular Docking*

Molecular docking analysis was performed to evaluate the interaction of synthesized unsymmetrical monocarbonyl curcuminoids with tubulin and to assess their potential as a tubulin-targeting anticancer agent. Docking study can predict protein–ligand interaction by profiling hydrogen bonding and hydrophobic, π-interactions within the binding cavity. In the present study, the synthesized unsymmetrical monocarbonyl curcuminoids were docked against tubulin (PDB ID: 6O5M), a structure containing a co-crystallized ligand bound to a colchicine-binding site [27].

To validate the docking protocol, the co-crystallized ligand, (2-(1*H*-indol-3-yl)-1*H*-imidazol-4-yl)(3,4,5-trimethoxyphenyl)methanone (ABI-231 analogue), was extracted from the native protein structure and redocked into its original binding site using the same grid parameters (60 × 60 × 60 Å, centered at x = 22.103, y = −76.640, and z = −50.798 Å). The redocked pose reproduced the experimental binding pose with a root mean square deviation (RMSD) of 0.746 Å, well within the threshold of <2.0 Å for a reliable docking protocol. The co-crystallized ligand occupied a binding cavity comprising Gly10, Gln11, Ala12, Gln15, Asp69, Asp98, Ala99, Ala100, Asn101, Ser140, Gly142, Gly143, Gly144, Ile171, Val177, Thr179, Glu183, Asn206, Tyr224, Leu227, Asn228, and Ile231, consistent with the reported the colchicine-binding site [28].

Docking of the synthesized curcuminoids revealed binding energies ranging from −8.38 to −9.04 kcal/mol (Table 1). Among the compounds investigated, **IMNP** showed the most favorable binding energy (−9.04 kcal/mol), followed by **CMND** (−8.96 kcal/mol), **CMNP** (−8.40 kcal/mol), and **MMND** (−8.38 kcal/mol).

**Table 1.** Docking analysis of monocarbonyl curcuminoids against tubulin (PDB ID: 6O5M).

| Compounds | Binding Energy (kcal/mol) |
|---|---|
| CMND | −8.96 |
| CMNP | −8.40 |
| MMND | −8.38 |
| IMNP | −9.04 |

All four compounds occupied a similar region of the colchicine-binding cavity, although differences in specific residue-level interactions were observed (Figure 1). The aromatic rings of these compounds interacted predominantly with non-polar regions of the cavity, while oxygen-containing functional groups were oriented toward residues capable of forming polar interactions; this combination of polar and non-polar contacts underlies the overall binding mode of the curcuminoid scaffold within the tubulin colchicine site.

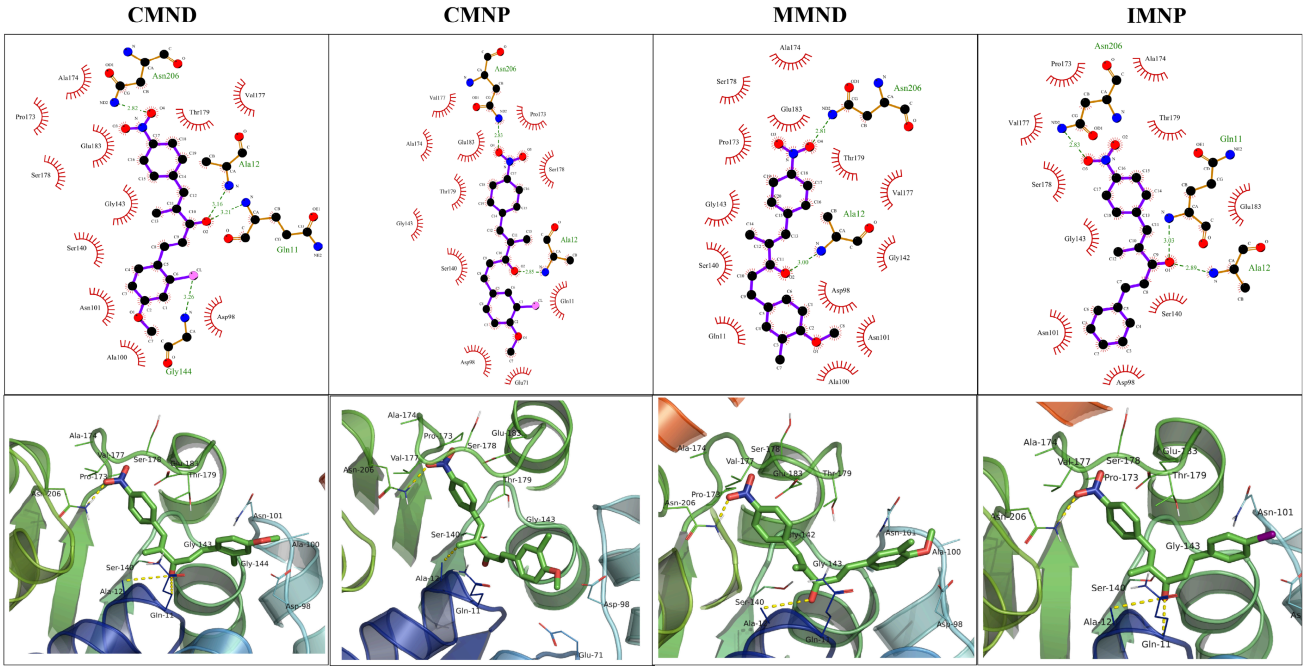



**Figure 1.** Docking interactions of the synthesized curcuminoids against tubulin (PDB ID: 6O5M).

Asn206 consistently established a hydrogen bond with all four investigated compounds, at distances ranging from 2.81 to 2.83 Å, indicating a conserved interaction across the series within binding cavity. Ala12 also consistently formed hydrogen bonds across all four complexes, with distances ranging from 2.85 to 3.16 Å; despite lacking a polar side chain, its backbone amino group consistently engaged in polar interaction with the carbonyl oxygen of the curcuminoid scaffold.

Additionally, **CMND** and **IMNP** each formed an additional hydrogen bond involving Gln11, which interacted with carbonyl oxygen of the perspective curcuminoid scaffold. Specifically, Gly144 was predicted to form a hydrogen bond with the chlorine substituent of **CMND**, an interaction that was absent in **CMNP**, despite **CMNP** being a closely related analogue containing the same chlorine substituent.

In addition to these polar interactions, all docked complexes showed hydrophobic and van der Waals interactions involving Val177, Pro173, Ala174, Thr179, Glu183, Gly143, Ser140, Asp98, Ala100, Asn101, Gly142, and Gln11, which further stabilized ligand positioning within the binding cavity. Overall, the aromatic core and heteroatoms of the curcuminoid scaffold establish a conserved binding mode across all four compounds, while differences

in substituent position produced distinct residue-level interactions, most notably at Gln11, where small structural modifications were found to influence overall binding behavior.

### *2.2. Molecular Dynamics Simulation*

The dynamic behavior of the four tubulin–ligand docked complexes and apo tubulin was investigated using 100 ns molecular dynamics (MD) simulations. Trajectories were analyzed via root mean square deviation (RMSD), radius of gyration (Rg), solvent-accessible surface area (SASA), root mean square fluctuation (RMSF), hydrogen-bond analysis, and MM-PBSA binding free-energy calculations.

RMSD was used to assess the conformational stability of apo tubulin and the four ligand-bound complexes across the 100 ns trajectory. As shown in Figure 2a, apo tubulin rapidly reached equilibrium after 5 ns and remained stable throughout the simulation. All four ligand-bound systems showed higher RMSD than the apo protein. The **CMNP–tubulin complex** showed the lowest fluctuations among the docked complexes, stabilizing at an RMSD of 0.70–0.85 nm after 8–10 ns. **CMND–tubulin** showed similar behavior, with RMSD values of 0.70–0.95 nm and a transient deviation between 40 and 50 ns. **IMNP–tubulin** exhibited greater fluctuation, with RMSD of 1.20–1.50 nm and pronounced fluctuations between 50 and 60 ns. **MMND–tubulin** showed the highest deviation among all complexes, with RMSD reaching 1.30–1.50 nm by 80 ns and increasing further to approximately 2 nm after 90 ns. **IMNP**, despite showing most favorable docking energy, did not display the lowest RMSD; instead, **CMNP**, with a comparatively moderate docking energy, showed the high dynamic stability.

Rg analysis was used to examine the compactness of tubulin during the simulation. Apo tubulin maintained an approximately constant Rg of 2.12–2.13 nm, reflecting preserved global structural compactness. The docked complexes showed similarly narrow ranges (2.09–2.14 nm). **CMND–tubulin** showed a moderate Rg increase between 20 and 70 ns. **CMNP–tubulin** and **MMND–tubulin** displayed slightly lower Rg (2.09–2.11 nm), while **IMNP–tubulin** remained relatively constant at 2.11–2.12 nm. Overall, the relatively narrow Rg ranges indicate that ligand binding did not produce large changes in the global compactness of the tubulin structure (Figure 2b).

RMSF was used to characterize the residue-level flexibility across the tubulin protein. The RMSF profile for apo tubulin and all docked complexes showed similar patterns, with most residues fluctuating below 0.10 nm. Prominent fluctuations were observed around residues 35–45, 170–180, 280–290, and the C-terminal region (430–440), consistently across all systems, with only modest differences between complexes: **CMND** showed increased flexibility around residues 280–290, while **IMNP** exhibited slightly higher fluctuations in the N-terminal region; **CMNP** and **MMND** displayed similar variation to one another. Maximum fluctuations reached approximately 0.35–0.37 nm, while most residues remained within 0.04–0.08 nm (Figure 2c).

SASA analysis was used to assess the solvent exposure of tubulin during the simulation. Apo tubulin maintained a SASA value of 230–236 $nm^2$, and the **CMND**, **MMND**, and **IMNP** complexes showed comparable values (229–236 $nm^2$). In contrast, the **CMNP–tubulin complex** showed a lower SASA (180–190 $nm^2$) throughout the simulation (Figure 2d), indicating reduced solvent exposure. However, its relatively unchanged radius of gyration (2.09–2.11 nm), compared with apo tubulin (2.12–2.13 nm) suggests that this reduction was not necessarily associated with global structural compaction. It may instead reflect localized changes in solvent accessibility. Nevertheless, specific conformational shifts or domain closures within the colchicine-binding pocket cannot be established from global SASA and Rg analyses alone. Further residue-level and structural investigations would be required to identify the underlying conformational changes.

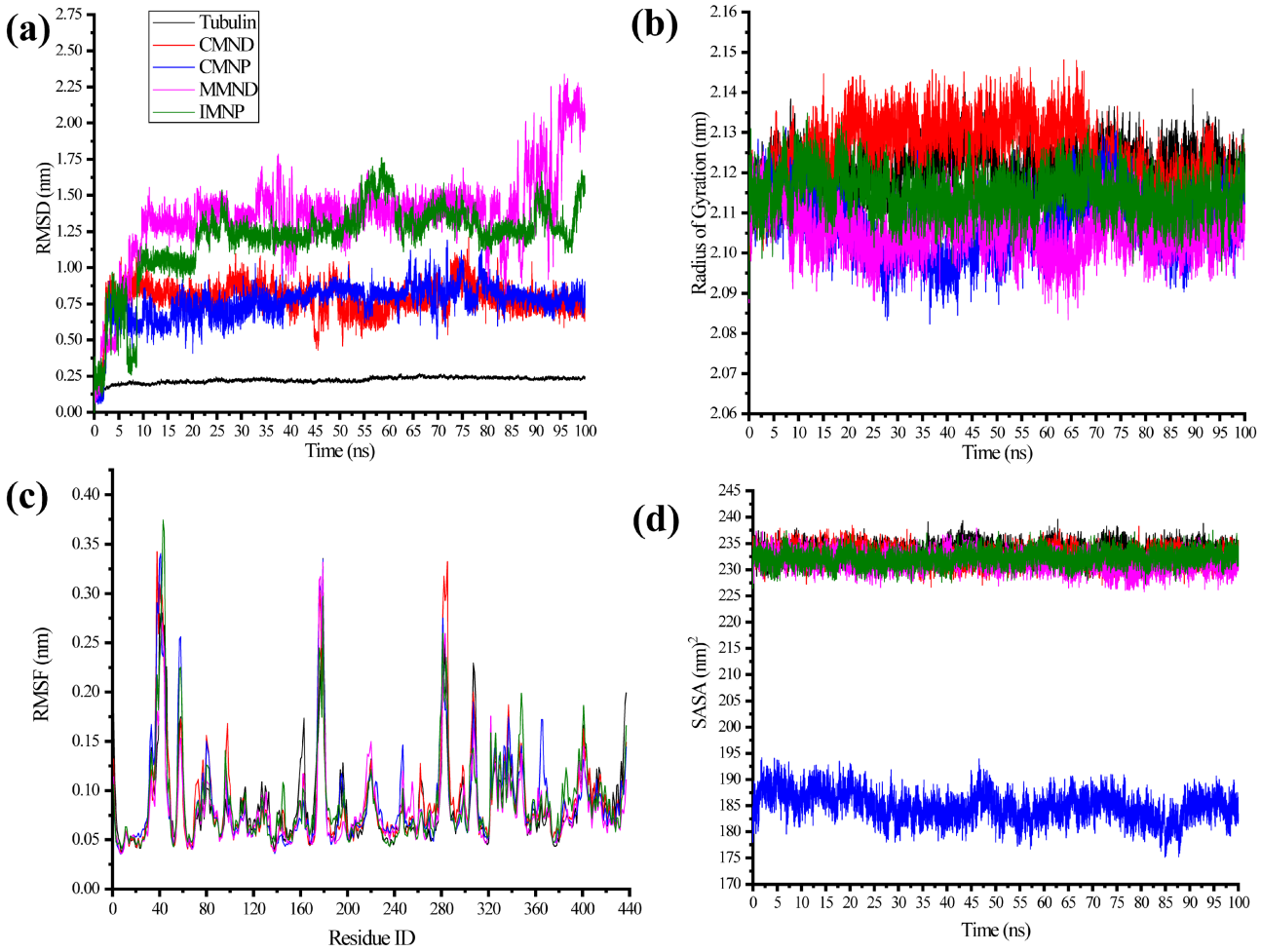



**Figure 2.** MD simulation of apo tubulin and tubulin–ligand docked complexes. (**a**) Root mean square deviation (RMSD), (**b**) radius of gyration (Rg), (**c**) root mean square fluctuation (RMSF), (**d**) solvent-accessible surface area (SASA).

Hydrogen-bond analysis assessed the persistence of directional protein–ligand interactions throughout the simulation. All four docked complexes retained hydrogen bonding contacts; however, the number of hydrogen bonds varied across the trajectory. **CMND–tubulin** maintained one to three hydrogen bonds, while **CMNP–tubulin** exhibited mainly one to three, with occasional formation of four simultaneous hydrogen bonds. **MMND–tubulin** showed one to two hydrogen bonds, with intermittent formation of three, while **IMNP–tubulin** maintained one to three hydrogen bonds, with occasional formation of four (Figure 3a).

MM-PBSA calculations were subsequently employed to obtain relative estimates of the binding energetics of the four tubulin–ligand complexes. All four docked complexes exhibited negative MM-PBSA binding free energy throughout their trajectories (Figure 3b). **CMNP–tubulin** exhibited the most favorable (most negative) MM-PBSA binding free energy, at ($\Delta G_{avg}$ = −20.9267 kcal/mol). **CMND–tubulin** showed a similar overall profile ($\Delta G_{avg}$ = −19.5282 kcal/mol), with some occasional variation. **IMNP–tubulin** displayed intermediate behavior ($\Delta G_{avg}$ = −19.0066 kcal/mol), which was more favorable than **MMND** but less favorable than **CMND** and **CMNP**.

MM-PBSA energy decomposition provides insight energetic contributions underlying the predicted binding of the four curcuminoids to tubulin (Table 2). All four docked complexes displayed favorable (negative) binding free energies, with **CMNP** showing the most favorable $\Delta G_{bind}$ (−20.93 ± 4.77 kcal/mol), followed by **CMND** (−19.53 ± 3.63 kcal/mol),

**IMNP** (−19.01 ± 3.83 kcal/mol), and **MMND** (−13.11 ± 3.65 kcal/mol). The most favorable **CMNP** was associated with its strong van der Waals (−32.32 ± 4.51 kcal/mol), electrostatic (−10.95 ± 6.66 kcal/mol), and non-polar solvation (−5.20 ± 0.68 kcal/mol) contributions. These interactions produced a highly favorable gas-phase energy ($\Delta G_{GAS}$ = −43.27 ± 7.64 kcal/mol), which was partially altered by the unfavorable polar solvation term ($\Delta E_{GB}$ = +27.54 ± 6.02 kcal/mol). **CMND** displayed a similar energetic pattern, with favorable van der Waals, electrostatic, and non-polar solvation contributions yielding an overall $\Delta G_{bind}$ of −19.53 ± 3.63 kcal/mol. **IMNP** likewise showed a favorable overall binding free energy (−19.01 ± 3.83 kcal/mol), despite weaker electrostatic and van der Waals contributions relative to **CMNP** and **CMND**. **MMND** exhibited the least favorable overall $\Delta G_{bind}$ (−13.11 ± 3.65 kcal/mol); this reduction was driven primarily by a weaker van der Waals contribution (−24.14 ± 4.55 kcal/mol) rather than by electrostatics, which were comparable to IMNP, indicating that reduced hydrophobic interactions rather than differences in polar contacts are the main factor underlying **MMND**'s comparatively weaker predicted binding affinity.

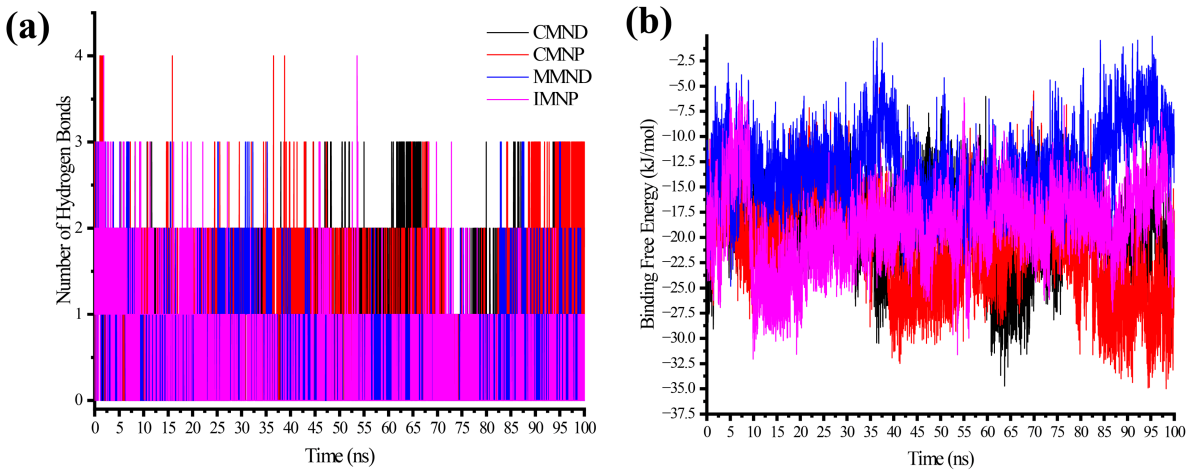



**Figure 3.** MD simulation of apo and tubulin–ligand docked complexes. (**a**) Number of intermolecular hydrogen bonds, (**b**) MM-PBSA binding free energy (kJ/mol).

**Table 2.** MM-PBSA energy decomposition of the tubulin–ligand complexes (kcal/mol).

| | CMND | CMNP | IMNP | MMND |
|---|---|---|---|---|
| **ΔVDWAALS** | −30.91 ± 3.78 | −32.32 ± 4.51 | −29.31 ± 4.49 | −24.14 ± 4.55 |
| **$\Delta E_{EL}$** | −10.42 ± 6.10 | −10.95 ± 6.66 | −6.93 ± 5.93 | −7.37 ± 6.06 |
| **$\Delta E_{GB}$** | 26.81 ± 5.99 | 27.54 ± 6.02 | 21.35 ± 7.58 | 22.23 ± 6.76 |
| **$\Delta E_{SURF}$** | −5.01 ± 0.51 | −5.20 ± 0.68 | −4.11 ± 0.73 | −3.83 ± 0.68 |
| **$\Delta G_{GAS}$** | −41.33 ± 7.88 | −43.27 ± 7.64 | −36.24 ± 8.68 | −31.51 ± 8.72 |
| **$\Delta G_{SOLV}$** | 21.81 ± 5.74 | 22.35 ± 5.99 | 17.24 ± 7.08 | 18.40 ± 6.32 |
| **$\Delta G_{bind}$** | −19.53 ± 3.63 | −20.93 ± 4.77 | −19.01 ± 3.83 | −13.11 ± 3.65 |

ΔVDWAALS, van der Waals contribution; $\Delta E_{EL}$, electrostatic contribution; $\Delta E_{GB}$, polar solvation contribution; $\Delta E_{SURF}$, non-polar solvation contribution; $\Delta G_{GAS}$, gas-phase contribution; $\Delta G_{SOLV}$, total solvation contribution; $\Delta G_{bind}$, estimated binding free energy.

Although 100 ns MD simulations provided insights into the dynamic behavior of the protein–ligand complexes, the pronounced RMSD increased observed in the **MMND**–tubulin complex during the final stage of the simulation suggest possible conformational drift and raise concerns regarding complete convergence. Subsequently, the calculated MM-PBSA binding free energies should be regarded as approximate, trajectory-dependent estimates rather than thermodynamic binding affinities. A duration longer

than 100 ns and independent replicas will be necessary to establish the reproducibility and convergence of the estimates.

### *2.3. DFT Study*

#### 2.3.1. Geometric Optimization

The molecular structures of **CMND**, **CMNP**, **MMND**, and **IMNP** were optimized at the ωb97xd/6-31+G(d,p) level of theory (Figure S9) [29]. Frequency calculations showed no imaginary frequencies, confirming that the optimized structures correspond to local minima on the potential energy surface.

#### 2.3.2. Frontier Molecular Orbital (FMO) Analysis

Frontier molecular orbitals (FMOs), the highest occupied molecular orbital (HOMO) and lowest unoccupied molecular orbital (LUMO), govern a molecule's electron-donating and electron-accepting behavior, respectively, and are central to understanding its electronic structure and intermolecular reactivity. Intramolecular charge transfer (ICT) occurs when electron-donating groups at peripheral molecular positions are connected to electron-accepting groups through a π-conjugated pathway, and the magnitude of the resulting HOMO–LUMO gap reflects the extent of this charge transfer [30,31].

HOMO and LUMO energies of CMND, CMNP, MMND, and IMNP were calculated at the ωB97X-D/6-31+G(d,p) level of theory [32], and the corresponding orbital distributions are shown in Figure 4. In the HOMO diagram, orbital density is localized primarily over the halogen-substituted benzene ring, while in the LUMO diagram, density is localized over the nitrobenzene moiety, indicating a shift in electron density from the halogenated aromatic ring toward the nitro-substituted ring upon excitation, consistent with the intramolecular charge-transfer character delocalized across the molecular structure [33].

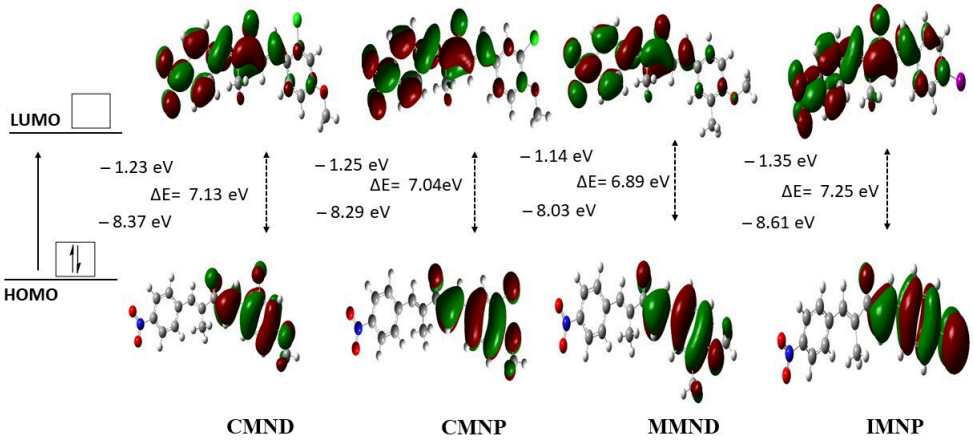



**Figure 4.** HOMO (**bottom**) and LUMO (**top**) isosurface (isovalue = 0.02 a.u.) and corresponding orbital energy levels (eV) of **CMND**, **CMNP**, **MMND**, and **IMNP**.

Reactivity descriptors, ionization potential ($I$), electron affinity ($A$), electronegativity ($\chi$), hardness ($\eta$), softness ($S$), chemical potential ($\mu$), and global electrophilicity index ($\omega$), were derived from the HOMO/LUMO energies using the following standard relationships [34]:

$$\Delta E = E_{LUMO} - E_{HOMO} \quad (1)$$

$$I = -E_{HOMO} \quad (2)$$

$$A = -E_{LUMO} \quad (3)$$

$$\chi = \frac{I + A}{2} \quad (4)$$

$$\mu = -\left(\frac{I + A}{2}\right) \quad (5)$$

$$\eta = -\left(\frac{I - A}{2}\right) \quad (6)$$

$$S = \frac{1}{2\eta} \quad (7)$$

$$\omega = \frac{\mu^2}{2\eta} \quad (8)$$

The calculated HOMO energies of **CMND**, **CMNP**, **MMND**, and **IMNP** were −8.37, −8.29, −8.03 and −8.61 eV, while the corresponding LUMO energies were −1.23, −1.25, −1.14 and −1.35 eV. The resulting HOMO-LUMO energy gaps ($\Delta E$) were 7.14, 7.04, 6.89 and 7.26 eV for **CMND**, **CMNP**, **MMND**, and **IMNP**, respectively. Among the four compounds, **MMND** showed the lowest HOMO-LUMO gap (6.89 eV), likely reflecting the stronger electron-donating character of its methoxy (-$OCH_3$) and methyl (-$CH_3$) substituents relative to the chlorine and iodine substituents present in **CMND**, **CMNP**, and **IMNP**, which more effectively donate electron density into the conjugated system, since a narrower HOMO-LUMO gap is generally associated with greater kinetic reactivity and lower kinetic stability [35]. **MMND** exhibited the smallest HOMO-LUMO gap (6.89 eV), suggesting greater kinetically reactivity and lower kinetic stability according to this descriptor. In contrast, the global electrophilicity index ($\omega$) was the highest for **IMNP** (3.42 eV), following by **CMND** and **CMNP** (3.23 eV each) and **MMND** (3.05 eV, Table 3).

**Table 3.** FMO energies and derived reactivity descriptors of **CMND**, **CMNP**, **MMND**, and **IMNP**.

| Parameters | CMND | CMNP | MMND | IMNP |
|---|---|---|---|---|
| $\mathbf{E_{HOMO}}$ **(eV)** | −8.37 | −8.29 | −8.03 | −8.61 |
| $\mathbf{E_{LUMO}}$ **(eV)** | −1.23 | −1.25 | −1.14 | −1.35 |
| **ΔE (eV)** | 7.14 | 7.04 | 6.89 | 7.26 |
| **I (eV)** | 8.37 | 8.29 | 8.03 | 8.61 |
| **A (eV)** | 1.23 | 1.25 | 1.14 | 1.35 |
| **S** ($\mathbf{eV^{-1}}$) | 0.14 | 0.14 | 0.15 | 0.14 |
| **χ (eV)** | 4.80 | 4.77 | 4.59 | 4.98 |
| **η (eV)** | 3.57 | 3.52 | 3.45 | 3.63 |
| **μ (eV)** | −4.80 | −4.77 | −4.59 | −4.98 |
| **ω (eV)** | 3.23 | 3.23 | 3.05 | 3.42 |

I, ionization potential; A, electron affinity; χ, electronegativity; η, chemical hardness; S, softness; μ, chemical potential; ω, global electrophilicity index.

The HOMO and LUMO orbitals of **CMND**, **CMNP**, **MMND**, and **IMNP** are shown in Figure 4. For **CMND**, electron density in the HOMO was concentrated over the aromatic ring bearing the chloro and methoxy substituents, whereas in the LUMO it redistributed toward the central dienone bridge and the nitro-substituted aromatic ring. A similar pattern, HOMO localization on the substituted (non-nitro) aryl ring, with LUMO density shifting toward the dienone bridge and nitrophenyl ring, was observed for **CMNP**, **MMND**, and **IMNP**, consistent with the shared 4-nitrophenyl group and cross-conjugated dienone core common to all four compounds, despite variation in the substituents on the second aryl ring (methoxy/methyl for **MMND**; iodo for **IMNP**).

Despite the smallest HOMO-LUMO energy gap (6.89 eV) of **MMND**, indicating greater electronic reactivity, this property does not correlate with stronger protein binding. Molecular binding affinity depends on factors such as steric effects, hydrogen bonding, hydrophobic interactions, and electrostatic contributions within the binding pocket. In the present study, **MMND** showed the least favorable predicted binding energy, primarily due to its weaker

van der Waals contribution (−24.14 ± 4.55 kcal/mol) compared with the other compounds. These findings demonstrate that electronic reactivity and protein-binding affinity represent distinct molecular properties.

#### 2.3.3. Molecular Electrostatic Potential (MEP) Surface Analysis

The molecular electrostatic potential (MEP) surface maps the electrostatic potential produced by a molecule's nuclei and electrons onto a molecular surface, representing the combined electrostatic contribution of both positively charged nuclei and negatively charged electrons. These regions help identify potential sites susceptible to nucleophilic or electrophilic attack and provide a useful complement to frontier orbital analysis for characterizing reactivity [35–37]. By convention, MEP surfaces are commonly displayed using a continuous color scale in which red denotes the most negative potential and blue the most positive potential. Regions of negative electrostatic potential are generally favorable sites susceptible to electrophilic attack, whereas regions of positive potential may favor the approach of nucleophilic species. Intermediate potentials are typically represented by colors such as orange, yellow, and green.

MEP surfaces for **CMND**, **CMNP**, **MMND**, and **IMNP** were computed in the gas phase at the ωB97X-D/6-31+G(d,p) level of theory (Figure 5). In all four compounds, the most negative potential (red) was predominantly localized over the oxygen atoms of the nitro and carbonyl groups, indicating regions of negative electrostatic potential that are favorable for the approach of electrophilic species. The most positive potential (blue) was distributed diffusely over the aromatic and vinylic C–H surface, indicating regions of positive electrostatic potential that may favor the approach of nucleophilic species. The halogen substituents (Cl in **CMND** and **CMNP**; I in **IMNP**) appeared within the intermediate (yellow-green) potential range, without exhibiting distinct high electrostatic regions. Overall, these observations characterize the electrostatic potential distribution across the compounds and support the findings of the FMO and NBO analysis.

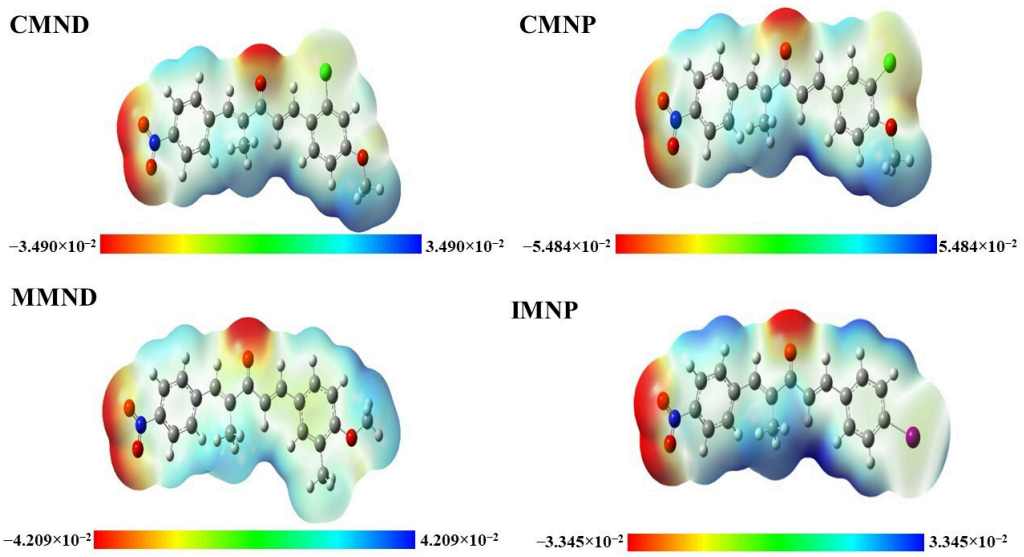



**Figure 5.** Molecular electrostatic potential (MEP) surfaces mapped onto an electron-density isosurface (isovalue = 0.001 a.u.) of **CMND**, **CMNP**, **MMND**, and **IMNP**. The color scale represents electrostatic potential in atomic units (a.u.).

#### 2.3.4. Electron Localization Function (ELF) and Localized Orbital Locator (LOL) Analysis

To further characterize the bonding and electron-pairing character of **CMND**, **CMNP**, **MMND**, and **IMNP**, electron localization function (ELF) and localized orbital locator

(LOL) analyses were performed using Multiwfn 3.8 software [29]. Electron localization descriptors provide a useful topological framework for interpreting chemical bonding. Both ELF and LOL are dimensionless topological descriptors [38–40], bounded between 0 and 1, that identify regions of space with a high probability of finding localized, same-spin-paired electrons; values approaching 1 (red) indicate strong electron localization, characteristic of covalent bonding regions and lone pairs, while values approaching 0 (blue) indicate electron delocalization, characteristic of the boundary between core and valence shells [41]. Electron localization is primarily associated with the Pauli exclusion principle, which reduces the probability of finding two same-spin electrons close together [42]. ELF describes this localization using information related to same-spin pair density and kinetic-energy density, with the homogeneous-electron-gas reference playing an important role in its formulation, while utilizes an inverse-gradient-based formulation stemming from the kinetic energy density ratio to yield a sharpened, alternative view of orbital localization boundaries and atomic shells [43,44].

ELF maps for **CMND**, **CMNP**, **MMND**, and **IMNP** are shown in Figure 6, as combined three-dimensional surface and two-dimensional contour representations. In all four compounds, localized domains (red/orange) appear concentrated over the bonding regions of the conjugated dienone backbone and the substituent-bearing aromatic rings, consistent with the delocalized π-system linking the two aryl groups, while lower-localization regions (blue/green) separate these bonding domains, marking boundaries between adjacent covalent/lone-pairs.

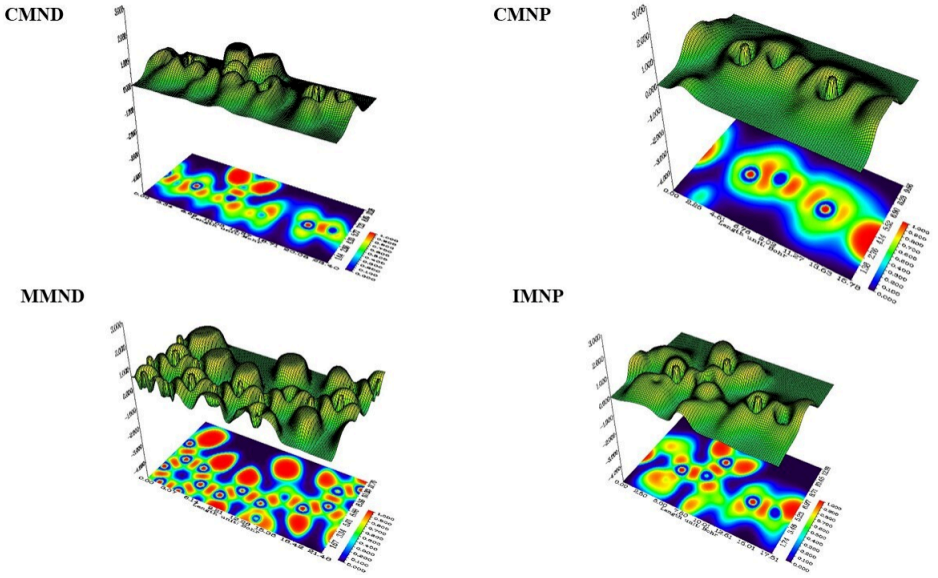



**Figure 6.** Electron localization function (ELF) surfaces (three-dimensional, (**top**)) and corresponding two-dimensional contour maps (**bottom**) of **CMND**, **CMNP**, **MMND**, and **IMNP**.

LOL maps (Figure 7) show a comparable pattern, with the color scale ranging from 0.000 (blue, delocalized) to 0.800 (red, strongly localized); the plotted spatial coordinates are given in Bohr (atomic units of length). Small blue rings immediately surrounding each nucleus mark the boundary between the core and valence electron shells, a signature feature common to all four compounds. Among the series, **MMND** displays the largest number of distinct, closely spaced localization basins, indicating a more spatially complex distribution of localized electron density across its conjugated framework, whereas **CMNP** and **IMNP** show fewer, more isolated basins. This greater degree of localized-electron-pair complexity in **MMND** is consistent with its comparatively narrow HOMO-LUMO gap and higher predicted reactivity reported in the FMO analysis above, suggesting that its

electronic structure supports a more delocalization-rich, reactive conjugated system than the other three compounds.

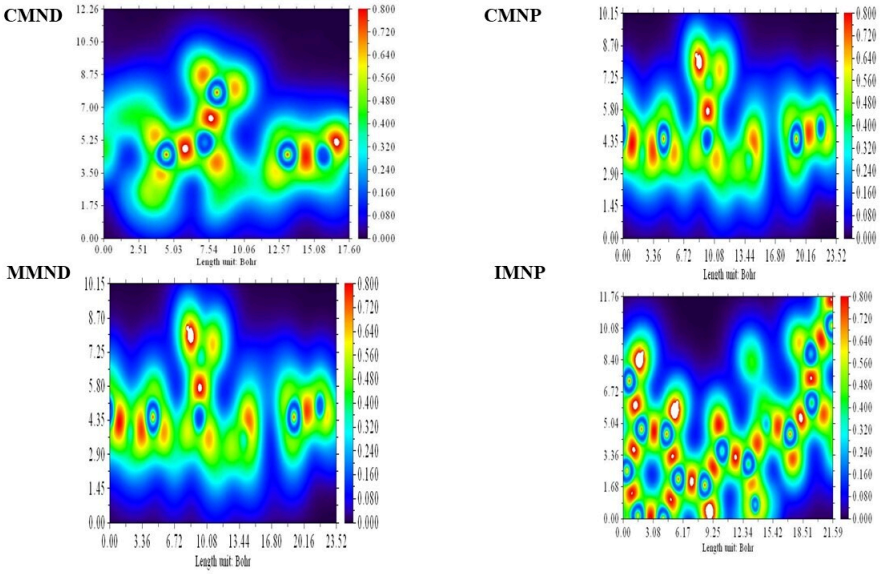



**Figure 7.** Localized orbital locator (LOL) two-dimensional contour maps of **CMND**, **CMNP**, **MMND**, and **IMNP**. Color scale ranges from 0.000 (blue, delocalized) to 0.800 (red, localized); spatial axes are given in Bohr (atomic units of length), representing the molecular cross-section analyzed.

### 2.3.5. Natural Bond Orbital (NBO) Analysis

NBO analysis provides a framework for investigating conjugative and charge transfer interaction between molecular systems by assessing inter- and intramolecular donor–acceptor orbital couplings. Second-order perturbation theory enables the quantification of these bond-antibonding delocalization interactions [45]. When an electron pair is transferred from a filled (donor) NBO to an empty or partially filled (acceptor) NBO, the resulting stabilizing energy, $E^{(2)}$, increases with the strength of interaction [46]. Lewis-type NBOs correspond to localized bonding orbitals ($\sigma$, $\pi$, or lone pairs), whereas non-Lewis NBOs correspond to empty antibonding ($\sigma^*$, $\pi^*$) orbitals [47]. NBO calculations were performed in Gaussian at the $\omega$B97X-D/6-31+G(d,p) level of theory to identify inter- and intramolecular hyperconjugative interactions, including lone pair-to-antibonding orbital donations. The second-order perturbation stabilization energy was calculated using Equation (9).

$$E^{(2)} = q_i \frac{\left(F_{i,j}\right)^2}{\varepsilon_j - \varepsilon_i} \quad (9)$$

where $q_i$ is the donor orbital occupancy, $F_{i,j}$ is the off-diagonal NBO Fock matrix element coupling donor $i$ and *acceptor* $j$, and $\varepsilon_i$ and $\varepsilon_j$ are the corresponding diagonal Fock matrix elements (orbital energies) of the donor and acceptor NBOs, respectively. Table 4 summarizes the principal $\sigma \rightarrow \sigma^*$, $\pi \rightarrow \pi^*$, and lone pair (LP)→antibonding donor–acceptor interactions for **CMND**, **CMNP**, **MMND**, and **IMNP**, along with their associated $E^{(2)}$ stabilization energies (kcal/mol). Across all four compounds, $\sigma \rightarrow \sigma^*$ interactions were comparatively weak, ranging from 0.50–0.57 kcal/mol (C29–O35→C26–C29 in **CMND**) up to 8.57–17.48 kcal/mol for the strongest $\sigma \rightarrow \sigma^*$ pair in each molecule (C14-H15→C16-C31 in **CMND** and **IMNP**; C38-H41→C38-H41 in **CMNP**; C41-H44→C41-H44 in **MMND**). $\pi \rightarrow \pi^*$ interactions comprised a similarly modest range for the weakest conjugative pathway in each compound (0.51–0.62 kcal/mol) but reached higher values (42.65–43.14 kcal/mol) for the C4–C5→C1–C6 (or structurally equivalent C27-C29→C23-C25) $\pi$-conjugation pathway

linking the central dienone bridge to the aromatic rings, consistent with delocalization across the extended π-system.

**Table 4.** NBO analysis of CMND, CMNP, MMND, and IMNP.

| Compound | Donor | Type | Acceptor | Type | $E^{(2)}$ (kcal/mol) | $E(j)$–$E(i)$ (a.u.) | $F(i,j)$ (a.u.) |
|---|---|---|---|---|---|---|---|
| **CMND** | C14-H15 | σ | C16-C31 | σ* | 8.72 | 1.09 | 0.087 |
| | C29-O35 | σ | C26-C29 | σ* | 0.50 | 1.66 | 0.026 |
| | C27-C29 | π | C23-C25 | π* | 43.02 | 0.39 | 0.117 |
| | C23-C25 | π | C23-C25 | π* | 0.52 | 0.39 | 0.013 |
| | O13 | LP2 | C6-H10 | σ* | 0.58 | 0.93 | 0.021 |
| | O18 | LP2 | C16-C17 | σ* | 25.47 | 0.83 | 0.132 |
| | Cl41 | LP3 | C24-C26 | π* | 16.92 | 0.46 | 0.085 |
| | O12 | LP3 | N11-O13 | π* | 245.04 | 0.22 | 0.210 |
| **CMNP** | C32-H34 | σ | C16-C32 | σ* | 0.51 | 1.10 | 0.021 |
| | C38-H41 | σ | C38-H41 | σ* | 14.96 | 4.65 | 0.236 |
| | C28-C30 | π | C28-C30 | π* | 0.62 | 0.38 | 0.014 |
| | C4-C5 | π | C1-C6 | π* | 42.81 | 0.37 | 0.113 |
| | Cl36 | LP3 | C23-C24 | σ* | 0.57 | 1.06 | 0.022 |
| | O18 | LP2 | C16-C17 | σ* | 25.13 | 0.84 | 0.132 |
| | Cl36 | LP3 | C24-C26 | π* | 16.12 | 0.45 | 0.083 |
| | O12 | LP2 | N11-O13 | π* | 244.89 | 0.22 | 0.210 |
| **MMND** | C28-C37 | σ | C37-H38 | σ* | 0.51 | 1.26 | 0.023 |
| | C41-H44 | σ | C41-H44 | σ* | 17.48 | 3.98 | 0.236 |
| | C19-C20 | π | C19-C20 | π* | 0.51 | 0.45 | 0.014 |
| | C4-C5 | π | C1-C6 | π* | 43.14 | 0.37 | 0.113 |
| | O35 | LP2 | C41-H43 | σ* | 0.54 | 3.72 | 0.042 |
| | O18 | LP2 | C16-C17 | σ* | 25.51 | 0.83 | 0.132 |
| | O35 | LP2 | C26-C30 | π* | 41.36 | 0.47 | 0.132 |
| | O12 | LP3 | N11-O13 | π* | 244.96 | 0.22 | 0.209 |
| **IMNP** | C17-C19 | σ | C19-H22 | σ* | 0.55 | 1.31 | 0.024 |
| | C14-H15 | σ | C16-C32 | σ* | 8.57 | 1.08 | 0.086 |
| | C26-C30 | π | C26-C30 | π* | 0.55 | 0.39 | 0.013 |
| | C4-C5 | π | C1-C6 | π* | 42.65 | 0.37 | 0.012 |
| | O13 | LP2 | C6-H10 | σ* | 0.57 | 0.94 | 0.021 |
| | O13 | LP2 | N11-O12 | σ* | 26.10 | 0.90 | 0.138 |
| | I37 | LP3 | C25-C28 | π* | 2.13 | 0.14 | 0.017 |
| | O12 | LP3 | N11-O13 | π* | 255.00 | 0.21 | 0.212 |

By far the most significant hyperconjugative interaction identified in all four compounds, however, was not among the σ→σ* or π→π* pathways but a lone pair-to-antibonding donation from a nitro-group oxygen into the adjacent N–O π* orbital (O12 LP→N11–O13 π*), with $E^{(2)}$ values of 245.04 (**CMND**), 244.89 (**CMNP**), 244.96 (**MMND**), and 255.00 kcal/mol (**IMNP**). This strong delocalization reflects extensive resonance donation from the nitro-oxygen lone pair into the N–O antibonding system, consistent with the classical resonance structure of the nitro group and directly corroborating two earlier findings: the concentration of the most negative electrostatic potential over the nitro oxygens in the MEP analysis. Additional moderately strong LP→antibonding interactions were observed for the methoxy/carbonyl oxygen donating into the adjacent aryl σ* system (O18 LP→C16-C17 σ*; $E^{(2)}$ = 25.1–26.1 kcal/mol across the series) and, where present, the halogen lone pairs donating into the adjacent aromatic π* system (Cl LP→π*, $E^{(2)}$ = 16.1–16.9 kcal/mol in **CMND**/**CMNP**; I LP→π*, $E^{(2)}$ = 2.13 kcal/mol in **IMNP**), the latter indicating comparatively weaker halogen-to-ring conjugation for the iodine substituent than for chlorine.

2.3.6. Natural Population Analysis (NPA)

Natural population analysis (NPA) offers a comparatively robust framework for partitioning molecular density into atomic charges and orbital population [48]. NPA provides insight into atomic charge distribution and can support interpretation of electrophilic and nucleophilic character through charge-based reactivity descriptors. It complements electrostatic-potential methods and other orbital-based analyses by offering an orbital-partitioning perspective on electron distribution [49]. Atoms that gain electron density acquire negative natural charges, whereas atoms that lose electron density acquire positive natural charges. These charge patterns provide a qualitative basis for identifying electron-deficient electrophilic ($E^+$) and electron-rich nucleophilic ($Nu^-$) sites [50]. Natural populations of **CMND**, **CMNP**, **MMND**, and **IMNP** at the same level of theory used throughout this study (ωB97X-D/6-31+G(d,p)) using the NBO program as implemented in Gaussian, and the resulting atomic natural charges and electronic configurations (core, valence, and Rydberg sub-shells) are provided in Supplementary Tables S5–S8.

Across all four compounds, natural charges followed a consistent element-dependent pattern: hydrogen atoms were uniformly positively charged, aromatic and vinylic carbons directly bonded to hydrogen, weakly positive to near-neutral, and carbons adjacent to electron-withdrawing groups in the cross-conjugated dienone bridge carried negative charges. Oxygen atoms were consistently negatively charged (approximately −0.3 to −0.6 *e*), as expected for their high electronegativity, with the carbonyl and nitro-group oxygens among the most electron-rich sites identified. Notably, the nitro-group nitrogen carried a strongly positive natural charge (+0.5 *e*) in every compound, reflecting substantial electron donation from nitrogen to its two bonded oxygens consistent with the dominant O(lone pair)→N–O(π*) hyperconjugative interaction identified in the NBO analysis above.

The single most negatively charged atom in each molecule, however, was not an oxygen atom but a carbon atom within the conjugated system (approximately −0.73 to −0.80 *e* across the series, exceeding the charge on any oxygen atom present). This finding indicates that the site of highest electron density in these molecules is a carbon center rather than a heteroatom, likely reflecting substantial π-electron delocalization from the aryl donor ring or the carbonyl oxygen into this position via the extended conjugated system, a pattern consistent with the strong π→π* delocalization energies (42.6–43.1 kcal/mol) identified in the NBO analysis (Figure 8).

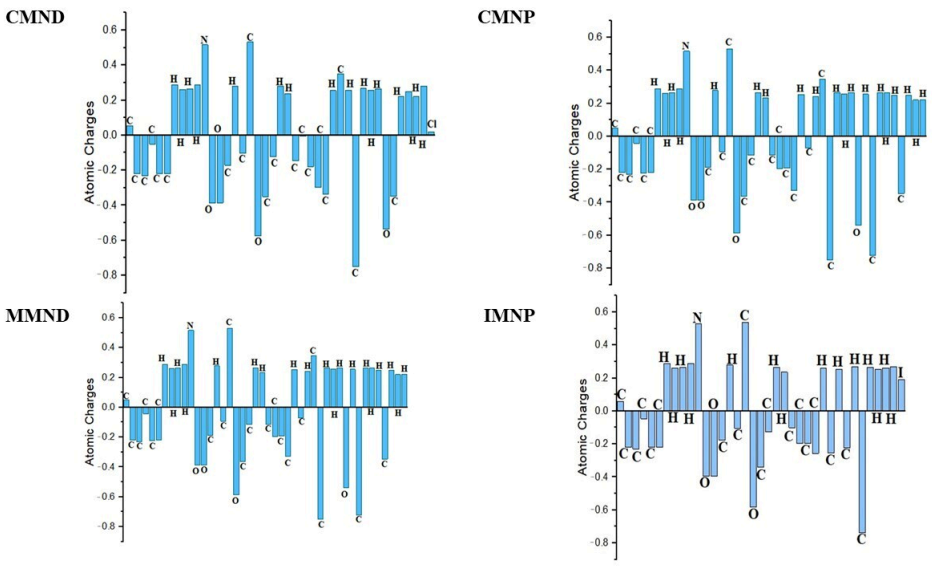



**Figure 8.** Natural population analysis (NPA) atomic charge distributions for **CMND**, **CMNP**, **MMND**, and **IMNP**.

2.3.7. Nonlinear Optical Properties (NLO)

Nonlinear optical (NLO) materials are of considerable interest because their light-induced optical responses support important applications in optical data storage, optical signal processing, and telecommunications [51]. Organic π-conjugated donor–acceptor chromophores are promising NLO materials because their extended electronic delocalization, strong intramolecular charge transfer, and tunable polarizability can produce pronounced nonlinear optical responses [52]. The static dipole moment ($\mu$), mean polarizability ($\alpha$), and first hyperpolarizability ($\beta$) of **CMND**, **CMNP**, **MMND**, and **IMNP** were computed in the gas phase using DFT, using the following standard relationships

$$\mu = \left(\mu_{x^2} + \mu_{y^2} + \mu_{z^2}\right)^{\frac{1}{2}} \tag{10}$$

$$a_{mean} = \frac{1}{3}\left(\alpha_{xx} + \alpha_{yy} + \alpha_{zz}\right) \tag{11}$$

$$\Delta\alpha = \frac{1}{\sqrt{2}}\left[\left(\alpha_{xx} - \alpha_{yy}\right)^2 + \left(\alpha_{yy} - \alpha_{zz}\right)^2 + \left(\alpha_{zz} - \alpha_{xx}\right)^2 + 6\alpha_{xz}^2\right]^{\frac{1}{2}} \tag{12}$$

$$\beta_{total} = \left[\left(\beta_{xxx} + \beta_{yyx} + \beta_{zzx}\right)^2 + \left(\beta_{yyy} + \beta_{xxy} + \beta_{zzy}\right)^2 + \left(\beta_{zzz} + \beta_{yyz} + \beta_{xxz}\right)^2\right]^{\frac{1}{2}} \tag{13}$$

All the values of NLO, such as dipole moment, polarizability and hyperpolarizability of the synthesized compounds mentioned in Table 5, are compared with urea. The dipole moments of CMND, CMNP, MMND and IMNP are 8.1263, 7.1105, 8.7991 and 362.2847 a.u, which are greater than urea's 4.56 D. The polarizability values for CMND, CMNP, MMND and IMNP are 292.7587, 297.5007, 298.7941 and 815.3809 a.u, respectively. These values are higher than the urea value of 30.49 a.u. The values of hyperpolarizability are 4629.1943, 5540.3957, 6290.4512 and 48,795.09877 for CMND, CMNP, MMND and IMNP, respectively.

**Table 5.** Computed dipole moment, polarizability, and first hyperpolarizability components of **CMND**, **CMNP**, **MMND**, and **IMNP**.

| | **CMND (a.s.u)** | **CMNP (a.s.u)** | **MMND (a.s.u)** | **IMNP (a.s.u)** |
|---|---|---|---|---|
| **Dipole moment ($\mu$) (Debye)** | | | | |
| $\mu_x$ | $2.92 \times 10^{-31}$ | $-4.89 \times 10^{-29}$ | $-7.56 \times 10^{-29}$ | $3.06 \times 10^{-27}$ |
| $\mu_y$ | $-3.90 \times 10^{-29}$ | $3.70 \times 10^{-29}$ | $7.21 \times 10^{-30}$ | $-6.45 \times 10^{-28}$ |
| $\mu_z$ | $2.92 \times 10^{-31}$ | $3.38 \times 10^{-30}$ | $3.29 \times 10^{-30}$ | $1.86 \times 10^{-29}$ |
| $\mu_{total}$ | $7.02 \times 10^{-29}$ | $6.14 \times 10^{-29}$ | $7.60 \times 10^{-29}$ | $3.12 \times 10^{-27}$ |
| **Polarizability ($\alpha$) (a.u)** | | | | |
| $\alpha_{xx}$ | $4.09 \times 10^{-27}$ | $4.34 \times 10^{-27}$ | $4.37 \times 10^{-27}$ | $1.02 \times 10^{-26}$ |
| $\alpha_{yy}$ | $2.26 \times 10^{-27}$ | $2.17 \times 10^{-27}$ | $2.14 \times 10^{-27}$ | $6.63 \times 10^{-27}$ |
| $\alpha_{zz}$ | $1.24 \times 10^{-27}$ | $1.20 \times 10^{-27}$ | $1.23 \times 10^{-27}$ | $4.28 \times 10^{-27}$ |
| $\alpha_{total}$ | $2.53 \times 10^{-27}$ | $2.57 \times 10^{-27}$ | $2.58 \times 10^{-27}$ | $7.04 \times 10^{-27}$ |
| **Hyperpolarizability ($\beta$) Å$^3$** | | | | |
| $\beta_{xxx}$ | $4.01 \times 10^{-26}$ | $4.44 \times 10^{-26}$ | $5.27 \times 10^{-26}$ | $2.46 \times 10^{-25}$ |
| $\beta_{xxy}$ | $8.39 \times 10^{-27}$ | $-9.82 \times 10^{-27}$ | $-8.98 \times 10^{-27}$ | $1.70 \times 10^{-25}$ |
| $\beta_{xyy}$ | $-1.51 \times 10^{-27}$ | $2.53 \times 10^{-27}$ | $1.00 \times 10^{-27}$ | $1.11 \times 10^{-25}$ |
| $\beta_{yyy}$ | $-1.04 \times 10^{-27}$ | $9.35 \times 10^{-29}$ | $-8.61 \times 10^{-28}$ | $-2.56 \times 10^{-25}$ |

**Table 5.** *Cont.*

| | **CMND (a.s.u)** | **CMNP (a.s.u)** | **MMND (a.s.u)** | **IMNP (a.s.u)** |
|---|---|---|---|---|
| $\beta_{xxz}$ | $-1.64 \times 10^{-27}$ | $-5.76 \times 10^{-28}$ | $-7.54 \times 10^{-28}$ | $-2.58 \times 10^{-25}$ |
| $\beta_{yyz}$ | $-2.54 \times 10^{-28}$ | $2.54 \times 10^{-29}$ | $4.14 \times 10^{-29}$ | $1.89 \times 10^{-25}$ |
| $\beta_{xzz}$ | $-9.79 \times 10^{-30}$ | $1.22 \times 10^{-30}$ | $-3.48 \times 10^{-28}$ | $-6.21 \times 10^{-25}$ |
| $\beta_{yzz}$ | $-3.21 \times 10^{-28}$ | $3.22 \times 10^{-28}$ | $-4.53 \times 10^{-28}$ | $-6.30 \times 10^{-26}$ |
| $\beta_{zzz}$ | $-4.79 \times 10^{-28}$ | $-8.81 \times 10^{-29}$ | $-1.00 \times 10^{-29}$ | $-2.23 \times 10^{-26}$ |
| $\beta_{total}$ | $4.01 \times 10^{-26}$ | $4.79 \times 10^{-26}$ | $5.43 \times 10^{-26}$ | $4.22 \times 10^{-25}$ |

#### 2.3.8. Vibrational Spectral Analysis

The vibrational characteristics of **CMND**, **CMNP**, **MMND**, and **IMNP** were evaluated using both experimental and theoretical FTIR spectroscopy. Theoretical vibrational frequencies and intensities were computed at the ωB97X-D/6-31+G(d,p) level of theory (Supplementary Tables S1–S4). Theoretical vibrational frequencies represent unscaled harmonic frequencies, as no scaling factor was applied. Therefore, differences between calculated and experimental frequencies may arise from the harmonic approximation and anharmonic effects. The following key vibrational modes were identified and compared between experimental and computed spectra.

**C=O vibrations:** The stretching modes of the C=O group are found in the 1850–1600 $cm^{-1}$ range [53]. Experimental C=O stretching bands were observed at 1664, 1660, 1650 $cm^{-1}$ for **CMND**, **CMNP**, **MMND**, and **IMNP**, respectively (Figures S1–S4), corresponded to computed values of 1799.29, 1801.07, 1796.47 and 1801.49 $cm^{-1}$ (Tables S1–S4).

**C-N vibrations:** The stretching modes of the C–N group are generally observed in the 1500–500 $cm^{-1}$ range [54]. Experimental bands were observed at 1510 to 1534 $cm^{-1}$ for the series (Figures S1–S4), corresponding to the DFT values of 1143.30, 1476.02, 912.74 and 908.03 $cm^{-1}$ (Tables S1–S4).

**C-H vibrations:** Aromatic C–H stretching modes are typically observed in the 3000–3100 $cm^{-1}$ spectral range [55]. The theoretically observed peak for C-H stretching is 2825–2949 $cm^{-1}$ (Tables S1–S4) for the series, corresponding to the experimental measurement at 3088–3070 $cm^{-1}$ (Figures S1–S4).

**C=C vibrations:** C=C stretching modes are generally observed between 1660 and 1600 $cm^{-1}$, with aromatic C=C modes appearing between 1600 and 1475 $cm^{-1}$. Computed C=C stretching frequencies were 1677.96, 1682.77, 1678.24 and 1714.77 $cm^{-1}$ for CMND, CMNP, MMND, and IMNP, respectively (Tables S1–S4). These computed values agreed with the experimental measurements at 1797, 1741, 1681 and 1658 $cm^{-1}$, respectively (Figures S1–S4).

## 3. Materials and Methods

### *3.1. Chemistry: Synthesis and Characterization*

All standard chemicals were purchased from reputable chemical suppliers, including Sigma-Aldrich (St. Louis, MO, USA), Macklin (Shanghai, China), Acros Chemicals (Geel, Belgium), and TCI (Tokyo, Japan). They were used as received without further purification. Reaction progress was monitored by thin layer chromatography (TLC) using pre-coated silica gel G-25-UV254 plates. Dry HCl gas, formed by the reaction of NaCl with concentrated $H_2SO_4$, was introduced into the reaction mixture through a glass delivery tube. The unsymmetrical monocarbonyl curcuminoid derivatives **CMND**, **CMNP**, **MMND**, and **IMNP** were synthesized via a two-step, acid-catalyzed aldol condensation approach

in a one-pot manner [56]. Dry HCl serves as an acid catalyst, encouraging two sequential aldol condensation reactions in a one-pot procedure without requiring the isolation of intermediate generated during the course of the first condensation step. This approach simplifies the synthetic pathway and improves operational efficiency compared to the conventional stepwise approaches involving an acid-catalyzed first aldol condensation, followed by a separate base-catalyzed second condensation step involving intermediate isolation [57–60]. The structures of all four derivatives were confirmed by $^{1}H$ and $^{13}C$ nuclear magnetic resonance (NMR) and infrared (IR) spectroscopy.

### *3.2. General Procedure*

Butanone and 4-nitro benzaldehyde were combined in a 1:1 ratio in a 50 mL two-necked round bottom flask containing 20 mL of dichloromethane. Dry HCl gas was passed through the mixture with stirring until the solution turned red, and stirring continued for 4 to 6 h, affording intermediate **3** in situ, as confirmed by TLC. One equivalent of aryl halide (specified below for each derivative) was added, and the reaction mixture was stirred for a further 5 h. Upon completion (monitored by TLC), the mixture was diluted with toluene and rinsed with aqueous $NaHSO_3$ solution. The organic layer was separated, and dried over anhydrous $Na_2SO_4$, and concentrated under reduced pressure using a rotary evaporator. The crude product was purified using column chromatography to afford the desired product.

#### 3.2.1. Compound CMND Was Obtained Using 2-Chloro-4-methoxybenzaldehyde as the Second Aldehyde, in 68% Isolated Yield

$^{1}H$ NMR (400 MHz, $CDCl_3$) δ 7.91 (dd, $J$ = 8.4, 1.9 Hz, 1H), 7.79 (d, $J$ = 1.9 Hz, 1H), 7.73 – 7.63 (m, 2H), 7.57 (d, $J$ = 8.4 Hz, 2H), 7.51 (d, $J$ = 8.4 Hz, 1H), 7.39 (dd, $J$ = 12.1, 5.7 Hz, 3H), 4.00 (s, 3H), 2.12 (s, 3H). $^{13}C$ NMR (100 MHz, $CDCl_3$) δ 192.0, 157.8, 148.6, 142.6, 141.0, 136.3, 133.5, 132.2, 131.7, 130.4, 129.5, 129.2, 122.1, 115.5, 105.6, 56.2, 14.1. IRύ$_{max}$, 3088, 1932, 1797, 1598, 1423 $cm^{-1}$.

#### 3.2.2. Compound CMNP Was Obtained Using 3-Chloro-4-methoxybenzaldehyde as the Second Aldehyde, in 67% Isolated Yield

$^{1}H$ NMR (400 MHz, $CDCl_3$) δ 8.30 (dd, $J$ = 9.0, 2.0 Hz, 2H), 7.94 (dd, $J$ = 8.3, 2.0 Hz, 1H), 7.84 – 7.79 (m, 2H), 7.79 – 7.73 (m, 2H), 7.71 (s, 1H), 7.57 – 7.50 (m, 2H), 4.02 (s, 3H), 2.14 (d, $J$ = 1.4 Hz, 3H). $^{13}C$ NMR (101 MHz, $CDCl_3$) δ 191.3, 157.8, 148.8, 148.5, 141.2, 140.9, 140.8, 133.1, 131.3, 130.5, 128.8, 125.3, 124.2, 115.6, 105.6, 56.2, 13.0. IRύ$_{max,}$ 3082, 1915, 1741, 1502, 1440 $cm^{-1}$.

#### 3.2.3. Compound MMND Was Obtained Using 3-Methyl-4-methoxybenzaldehyde as the Second Aldehyde, in 65% Isolated Yield

$^{1}H$ NMR (400 MHz, $CDCl_3$) δ 8.05 – 7.99 (m, 1H), 7.90 (dt, $J$ = 8.0, 4.0 Hz, 1H), 7.78 (m, 1H), 7.65 (s, 1H), 7.49 (m 2H), 7.26 (dd, $J$ = 7.9, 1.2 Hz, 1H), 7.10 (m, 1H), 6.98 (dd, $J$ = 8.1, 1.4 Hz, 1H), 3.99 (s, 3H), 3.90 (s, 3H), 2.12 (s, 3H). $^{13}C$ NMR (101 MHz, $CDCl_3$) δ 191.98, 158.63, 149.48, 147.36, 142.35, 141.39, 137.28, 136.01, 130.28, 129.09, 127.83, 125.58, 123.77, 115.89, 106.31, 56.30, 40.42, 14.03. IRύ$_{max}$ 3070, 1911, 1681, 1556, 1494 $cm^{-1}$.

#### 3.2.4. Compound IMNP Was Obtained Using 4-Iodobenzaldehyde as the Second Aldehyde, in 70% Isolated Yield

$^{1}H$ NMR (400 MHz, $CDCl_3$) δ 8.34 – 8.27 (m, 2H), 7.69 (d, $J$ = 15.6 Hz, 1H), 7.63 – 7.59 (m, 2H), 7.59 – 7.54 (m, 3H), 7.53 – 7.48 (m, 2H), 7.42 – 7.35 (m, 1H), 2.21 (dd, $J$ = 7.2,

1.4 Hz, 3H). $^{13}$C NMR (101 MHz, $CDCl_3$) δ 191.8, 147.3, 143.2, 142.4, 141.5, 135.5, 133.7, 132.2, 130.3, 129.8, 124.8, 123.8, 121.8, 14.1. IRύ$_{max,}$ 3084, 1907, 1658, 1587, 1469 cm$^{-1}$.

### *3.3. Computational Methodology*

The density functional theory (DFT) was computed using the Gaussian 09 program [61]. The molecular structures of **CMND**, **CMNP**, **MMND** and **IMNP** were fully optimized utilizing the ωb97xd/6-31 G+(d,p) level of theory in the gas phase. Vibrational frequency calculations confirmed that no imaginary frequencies were present, verifying that the optimized geometries represent true energy minima on the potential energy surface. The energies of the highest occupied molecular orbital (HOMO) and the lowest unoccupied molecular orbital (LUMO), and the HOMO-LUMO energy gap, were calculated and used to derive global reactivity descriptors. Topological analysis, including the electron localization function (ELF) and localized orbital locator (LOL), was performed using Multiwfn software (3.8) [62]. Natural population analysis (NPA) and natural bond orbital analysis (NBO) were conducted, and nonlinear optical (NLO) parameters were also computed. Theoretical UV–visible absorption spectra were generated using GaussSum program version 3.0 [63].

### *3.4. Molecular Docking Protocol*

Molecular docking was performed using AutoDock 4.2 with MGLTools/AutoDock tools [64]. The crystal structure of tubulin (PDB ID: 6O5M, resolution 2.30 Å) was retrieved from the RCSB Protein Data Bank (https://www.rcsb.org/). Prior to docking, the protein structure was prepared by removing the crystallographic water molecules, adding polar hydrogen, and assigning Kollman charges. Ligand structures were prepared by merging non-polar hydrogens, assigning Gasteiger charges, and defined rotatable bonds. A grid box of 60 × 60 × 60 Å with a spacing 0.375 Å, centered at x = 22.103, y = −76.640, and z = −50.798 Å, was used to cover the experimentally characterized colchicine-binding region. The docking protocol was validated by redocking the co-crystallized ligand into its native binding site using the same grid parameters. Docking of the synthesized curcuminoid derivatives (**CMND**, **CMNP**, **MMND**, and **IMNP**) was then performed using the validated parameters and the Lamarckian Genetic Algorithm (LGA), with a population size of 150, a maximum of 2,500,000 energy evaluations, and 27,000 generations. Ten independent docking runs were performed for each ligand and the pose with the lowest energy was selected as representative binding mode. Protein–ligand interactions were visualized using LigPlot+ (LigPlus) for two-dimensional diagrams [65], and PyMol for three-dimensional visualization [66].

### *3.5. Molecular Dynamics Simulations*

Molecular dynamics (MD) simulations were performed using GROMACS version 2021.4 [67] to evaluate the structural stability and dynamic behavior of the protein–ligand complexes obtained from molecular docking. Ligand topologies were generated using the SwissParam online server (https://old.swissparam.ch/), and protein topologies were prepared using the CHARMM27 force field in combination with the TIP3P explicit water model [68]. Each protein–ligand complex was solvated in a cubic simulation box with a minimum 10 Å solute-boundary distance, and the system was neutralized by the addition of sodium and chloride counterions. Energy minimization was performed using the steepest-descent algorithm to remove steric clashes, followed by system equilibration and a 100 ns production simulation under isothermal–isobaric (NPT) ensemble conditions. Post-simulation trajectory analyses included root mean square deviation (RMSD), root mean square fluctuation (RMSF), radius of gyration (Rg), solvent-accessible surface area

(SASA), and the number of intermolecular hydrogen bonds, to assess the structural stability and flexibility of each complex over the course of the simulation.

### *3.6. Binding Free Energy (MM-PBSA) Calculations*

Binding free energies ($\Delta G_{bind}$) of the protein–ligand complexes were estimated using the g_mmpbsa package (v1.6.3) [69–72]. Snapshots were extracted from the equilibrated 100 ns trajectories, sampling frames 1–5000 at one-frame intervals after removal of water molecules and ions. The MM-PBSA method was applied using an internal dielectric constant of 1.0, an external dielectric constant of 78.5, and a solvent probe radius of 1.4 Å. Non-polar solvation energy was estimated from the solvent-accessible surface area, and entropic contributions were not included due to high computational cost. The binding free energy was calculated as:

$$\Delta G_{bind} = G_{complex} - \left(G_{protein} + G_{ligand}\right) \quad (14)$$

where $G_{complex}$, $G_{protein}$, and $G_{ligand}$ represent the free energies of the complex, the isolated protein, and the isolated ligand, respectively.

## 4. Conclusions

The four unsymmetrical monocarbonyl curcuminoids, **CMND**, **CMNP**, **MMND**, and **IMNP**, were successfully afforded via one-pot, acid-catalyzed two-step aldol condensation and structurally characterized by spectroscopic methods. The integrated computational approach gave insights into electronic properties and potential interaction tubulin. Docking analysis showed the all four compounds can occupy the colchicine-binding site, with **IMNP** exhibiting the most favorable predicted docking energy. However, the 100 ns MD simulations demonstrated that MD and docking provide the complementary measure of binding stability. **CMNP** exhibited the most favorable dynamic profile, which was further supported by MM-PBSA binding free energy ($-20.93 \pm 4.77$ kcal/mol), followed by **CMND**, **IMNP**, and **MMND**. The results identify **CMNP** as the lead compounds among the series on the basis of combined docking and dynamic analysis.

DFT calculations revealed significant electronic delocalization and intramolecular charge transfer across the conjugated dienone-aryl structure. Among the investigated compounds, **MMND** exhibited the smallest HOMO-LUMO gap (6.89 eV), indicating comparatively greater kinetic reactivity. The MEP, ELF, LOL, NBO, and NPA analyses further characterized the electronic distribution and bonding behavior of the molecules, while calculated polarizability and hyperpolarizability values indicated potentially significant nonlinear optical properties. Furthermore, the different computational approaches did not produce an identical compound ranking. On the basis of the present computational results, **CMNP** represents the most promising candidate for further investigation as an anticancer agent.

**Supplementary Materials:** The following supporting information can be downloaded at https://www.mdpi.com/article/10.3390/catal16121071/s1, Figure S1-A: Experimental FTIR spectrum of the compound CMND; Figure S1-B: Computed FTIR spectrum of the compound CMND; Figure S2-A: Experimental FTIR spectrum of the compound CMNP, Figure S2-B: Computed FTIR spectrum of the compound CMNP; Figure S3-A: Experimental FTIR spectrum of the compound MMND; Figure S3-B: Computed FTIR spectrum of the compound MMND; Figure S4-A: Experimental FTIR spectrum of the compound IMNP; Figure S4-B: Computed FTIR spectrum of the compound IMNP; Figure S5: $^{1}$H and $^{13}$C spectra of compound CMND in $CDCl_3$; Figure S6: $^{1}$H and $^{13}$C spectra of compound CMNP in $CDCl_3$; Figure S7: $^{1}$H and $^{13}$C spectra of compound MMND in $CDCl_3$; Figure S8: $^{1}$H and $^{13}$C spectra of compound IMNP in $CDCl_3$; Figure S9: The optimized molecular structures of CMND, CMNP, MMND, and IMNP at ωb97xd/6-31+G(d,p) level of theory; Table S1: Calculated FTIR analysis of compound CMND; Table S2: Calculated FTIR analysis of compound CMNP; Table S3: Calculated

FTIR analysis of compound MMND; Table S4: Calculated FTIR analysis of compound IMNP; Table S5: Calculated NPA analysis of compound CMND; Table S6: Calculated NPA analysis of compound CMNP; Table S7: Calculated NPA analysis of compound MMND; Table S8: Calculated NPA analysis of compound IMNP.

**Author Contributions:** W.R.: Conceptualization, Methodology, Investigation, Data curation, Formal analysis, Visualization, Software, Writing—Original draft preparation. A.A.: Conceptualization, Supervision, Validation, Resources, Funding acquisition, Project administration, Writing—Reviewing and Editing. All authors have read and agreed to the published version of the manuscript.

**Funding:** This research received no external funding.

**Data Availability Statement:** The data related to this article is available in the manuscript and Supplementary Materials.

**Acknowledgments:** We are very thankful to Ajaz Hussain (Bahauddin Zakariya University, Multan, Pakistan) for providing the theoretical lab facilities for DFT study and guiding us through the computational analysis. We are also thankful to Musrat Shaheen and Shahzaib Akhtar for their valuable suggestions regarding computational investigation.

**Conflicts of Interest:** The authors declare no conflicts of interest.

## References

1. Sung, H.; Filho, A.M.; Laversanne, M.; Ferlay, J.; Siegel, R.L.; Soerjomataram, I. Global cancer statistics 2024: GLOBOCAN estimates of incidence and mortality worldwide for 34 cancers in 186 countries. *CA Cancer J. Clin.* **2026**, *76*, e70090. [CrossRef] [PubMed]
2. Ku, K.S.; Tang, J.; Chen, Y.; Shi, Y. Current advancements in anti-cancer chimeric antigen receptor T cell immunotherapy and how nanotechnology may change the game. *Int. J. Mol. Sci.* **2024**, *25*, 5361. [CrossRef] [PubMed]
3. Jordan, M.A.; Kamath, K. How do microtubule-targeted drugs work? An overview. *Curr. Cancer Drug Targets* **2007**, *7*, 730–742. [CrossRef] [PubMed]
4. Jordan, M.A. Mechanism of action of antitumor drugs that interact with microtubules and tubulin. *Curr. Med. Chem. Anticancer Agents* **2002**, *2*, 1–17. [CrossRef] [PubMed]
5. Lu, Y.; Chen, J.; Xiao, M.; Li, W.; Miller, D.D. An overview of tubulin inhibitors that interact with the colchicine binding site. *Pharm. Res.* **2012**, *29*, 2943–2971. [CrossRef] [PubMed]
6. Huang, L.; Peng, Y.; Tao, X.; Ding, X.; Li, R.; Jiang, Y.; Zuo, W. Microtubule organization is essential for maintaining cellular morphology and function. *Oxid. Med. Cell. Longev.* **2022**, *2022*, 1623181. [CrossRef] [PubMed]
7. Ilan, Y. Microtubules as a potential platform for energy transfer in biological systems: A target for implementing individualized, dynamic variability patterns to improve organ function. *Mol. Cell. Biochem.* **2023**, *478*, 375–392. [CrossRef] [PubMed]
8. Salinas, Y.; Chauhan, S.C.; Bandyopadhyay, D. Small-molecule mitotic inhibitors as anticancer agents: Discovery, classification, mechanisms of action, and clinical trials. *Int. J. Mol. Sci.* **2025**, *26*, 3279. [CrossRef] [PubMed]
9. Naaz, F.; Haider, M.R.; Shafi, S.; Yar, M.S. Anti-tubulin agents of natural origin: Targeting taxol, vinca, and colchicine binding domains. *Eur. J. Med. Chem.* **2019**, *171*, 310–331. [CrossRef] [PubMed]
10. Li, L.; Jiang, S.; Li, X.; Liu, Y.; Su, J.; Chen, J. Recent advances in trimethoxyphenyl (TMP) based tubulin inhibitors targeting the colchicine binding site. *Eur. J. Med. Chem.* **2018**, *151*, 482–494. [CrossRef] [PubMed]
11. Montecinos, F.; Sackett, D.L. Structural changes, biological consequences, and repurposing of colchicine site ligands. *Biomolecules* **2023**, *13*, 834. [CrossRef] [PubMed]
12. Xie, Y.; Hou, R.; Albadari, N.; Chen, H.; Miller, D.J.; Quadrozzi Gruntz, J.; Oldham, M.L.; Kamal, M.S.; Jiang, J.; Wu, Z.; et al. QW-5-70 targets the colchicine site and demonstrates antitumor activity in P-gp-overexpressing cancer models. *Mol. Cancer Ther.* **2026**, *25*, OF1–OF14. [CrossRef] [PubMed]
13. Colorado-Pablo, L.F.; Mar-Antonio, E.; Goode-Romero, G.; Morrissette, N.; Aguayo-Ortiz, R. Tubulin zone occupancy by PDB-deposited colchicine binding site inhibitors. *J. Med. Chem.* **2026**, *69*, 8650–8687. [CrossRef] [PubMed]
14. Sohn, S.I.; Priya, A.; Balasubramaniam, B.; Muthuramalingam, P.; Sivasankar, C.; Selvaraj, A.; Valliammai, A.; Jothi, R.; Pandian, S. Biomedical applications and bioavailability of curcumin—An updated overview. *Pharmaceutics* **2021**, *13*, 2102. [CrossRef] [PubMed]
15. Mishra, A.P.; Swetanshu; Singh, P.; Yadav, S.; Nigam, M.; Seidel, V.; Rodrigues, C.F. Role of the dietary phytochemical curcumin in targeting cancer cell signalling pathways. *Plants* **2023**, *12*, 1782. [CrossRef] [PubMed]

16. Yang, H.; Xiong, X.; Chen, X.; Huang, S.; Dai, H.; Yuan, L.; Fan, J.; Xiang, Z.; Wang, W.; Qin, Y. A mitochondrion-targeted natural polyphenolic copper carrier overcomes tumor resistance to cisplatin by potentiating cuproptosis. *J. Exp. Clin. Cancer Res.* **2026**, *45*, 53. [CrossRef] [PubMed]
17. Cao, M.; Wang, W.; Yang, X.; Zhu, W.; Zhu, X.; He, Y.; Chen, F.; Han, X. A dual-functional curcumin strategy for light scattering mitigation in high-fidelity DLP ceramic 3D printing. *Int. J. Extrem. Manuf.* **2026**, *8*, 055101. [CrossRef]
18. Liu, Z.; Smart, J.D.; Pannala, A.S. Recent developments in formulation design for improving oral bioavailability of curcumin: A review. *J. Drug Deliv. Sci. Technol.* **2020**, *60*, 102082. [CrossRef]
19. Wu, H.; Zhang, X.; Shu, X.; Zhang, H.; Zhou, W.; Zhang, S.; Luo, C. Molecularly tailored artesunate nanomedicine with well-balanced nanoassembly and anticancer performance. *Pharmaceutics* **2026**, *18*, 240. [CrossRef] [PubMed]
20. Nagargoje, A.A.; Panchgalle, S.P.; Siddiqui, M.M.; Shaikh, M.H.; More, D.; Shingate, B.B. Recent advances in the biological activities of monocarbonyl curcumin analogues (MACs). *Arch. Pharm.* **2025**, *358*, e70164. [CrossRef] [PubMed]
21. Kaur, K.; Al-Khazaleh, A.K.; Bhuyan, D.J.; Li, F.; Li, C.G. A review of recent curcumin analogues and their antioxidant, anti-inflammatory, and anticancer activities. *Antioxidants* **2024**, *13*, 1092. [CrossRef] [PubMed]
22. Bhandari, S.V.; Kuthe, P.; Patil, S.M.; Nagras, O.; Sarkate, A.P. A review: Exploring synthetic schemes and structure-activity relationship (SAR) studies of mono-carbonyl curcumin analogues for cytotoxicity inhibitory anticancer activity. *Curr. Org. Synth.* **2023**, *20*, 821–837. [CrossRef] [PubMed]
23. Nguyen, H.V.; Pham, V.T.B.; Hoang, H.M. Cytotoxicity of aromatic substituted curcuminoid against human lung cancer cell line. *Chiang Mai J. Sci.* **2021**, *48*, 1313–1321.
24. Kobylka, P.; Murias, M.; Kandulski, K.; Kucinska, M. Beyond curcumin: Structural modification strategies to improve stability, bioavailability, and antiproliferative activity. *Planta Med.* **2026**, *92*, 1152–1166. [CrossRef] [PubMed]
25. Chakraborti, S.; Das, L.; Kapoor, N.; Das, A.; Dwivedi, V.; Poddar, A.; Chakraborti, G.; Janik, M.; Basu, G.; Panda, D.; et al. Curcumin recognizes a unique binding site of tubulin. *J. Med. Chem.* **2011**, *54*, 6183–6196. [CrossRef] [PubMed]
26. Sharma, S.; Gupta, M.K.; Saxena, A.K.; Bedi, P.M.S. Triazole linked mono carbonyl curcumin-isatin bifunctional hybrids as novel anti tubulin agents: Design, synthesis, biological evaluation and molecular modeling studies. *Bioorg. Med. Chem.* **2015**, *23*, 7165–7180. [CrossRef] [PubMed]
27. Wang, Q.; Arnst, K.E.; Wang, Y.; Kumar, G.; Ma, D.; White, S.W.; Miller, D.D.; Li, W.; Li, W. Structure-guided design, synthesis, and biological evaluation of (2-(1H-indol-3-yl)-1H-imidazol-4-yl)(3,4,5-trimethoxyphenyl)methanone (ABI-231) analogues targeting the colchicine binding site in tubulin. *J. Med. Chem.* **2019**, *62*, 6734–6750. [CrossRef] [PubMed]
28. Boyles, F.; Deane, C.M.; Morris, G.M. Learning from docked ligands: Ligand-based features rescue structure-based scoring functions when trained on docked poses. *J. Chem. Inf. Model.* **2022**, *62*, 5329–5341. [CrossRef] [PubMed]
29. Chen, Z.; Li, Y.; He, Z.; Xu, Y.; Yu, W. Theoretical investigations on charge transport properties of tetrabenzo[a,d,j,m]coronene derivatives using different density functional theory functionals (B3LYP, M06-2X, and wB97XD). *J. Chem. Res.* **2019**, *43*, 293–303. [CrossRef]
30. Taouali, W.; Alimi, K.; Sindhoo Nangraj, A.; Casida, M.E. Density-functional theory (DFT) and time-dependent DFT study of the chemical and physical origins of key photoproperties of end-group derivatives of a nonfullerene acceptor molecule for bulk heterojunction organic solar cells. *J. Comput. Chem.* **2023**, *44*, 2130–2148. [CrossRef] [PubMed]
31. Asad , U.; Muhammad, I.; Afifa , Y.; Muhammad Arif, A.; Hongliang, X.; Muhammad, A. The interplay of electron push–pull dynamics and $\pi$-conjugation in non–linear optics. *Next Mater.* **2025**, *9*, 101239. [CrossRef]
32. Dege, N.; Şenyüz, N.; Batı, H.; Gunay, N.; Avcl, D.; Tamar, Ö.; Atalay, Y. The synthesis, characterization and theoretical study on nicotinic acid [1-(2,3-dihydroxyphenyl)methylidene]hydrazide. *Spectrochim. Acta A Mol. Biomol. Spectrosc.* **2014**, *120*, 323–331. [CrossRef] [PubMed]
33. Alghamdi, S.K.; Abbas, F.; Hussein, R.K.; Alhamzani, A.G.; El-Shamy, N.T. Spectroscopic characterization (IR, UV-Vis), and HOMO-LUMO, MEP, NLO, NBO analysis and the antifungal activity for 4-bromo-N-(2-nitrophenyl)benzamide using DFT modeling and in silico molecular docking. *J. Mol. Struct.* **2023**, *1271*, 134001. [CrossRef]
34. Dege, N.; Gökce, H.; Doğan, O.E.; Alpaslan, G.; Agar, T.; Muthu, S.; Sert, Y. Quantum computational, spectroscopic investigations on N-(2-((2-chloro-4,5-dicyanophenyl)amino)ethyl)-4-methylbenzenesulfonamide by DFT/TD-DFT with different solvents, molecular docking and drug-likeness researches. *Colloids Surf. A Physicochem. Eng. Asp.* **2022**, *638*, 128311. [CrossRef]
35. Suresh, C.H.; Remya, G.S.; Anjalikrishna, P.K. Molecular electrostatic potential analysis: A powerful tool to interpret and predict chemical reactivity. *WIREs Comput. Mol. Sci.* **2022**, *12*, e1601. [CrossRef]
36. Gadre, S.R.; Kumar, A. Bonding and reactivity patterns from electrostatic landscapes of molecules. *J. Chem. Sci.* **2016**, *128*, 1519–1526. [CrossRef]
37. Gadre, S.R.; Suresh, C.H.; Mohan, N. Electrostatic potential topology for probing molecular structure, bonding and reactivity. *Molecules* **2021**, *26*, 3289. [CrossRef] [PubMed]
38. Jacobsen, H. Localized-orbital locator (LOL) profiles of chemical bonding. *Can. J. Chem.* **2008**, *86*, 695–702. [CrossRef]

39. Clements, R.J.; Womack, J.C.; Skylaris, C.-K. Electron localisation descriptors in ONETEP: A tool for interpreting localisation and bonding in large-scale DFT calculations. *Electron. Struct.* **2020**, *2*, 027001. [CrossRef]
40. Janani, S.; Rajagopal, H.; Muthu, S.; Javed, S.; Irfan, A. Structural, electronic properties (different solvents), chemical reactivity, ELF, LOL, spectroscopic insights, molecular docking and in vitro anticancer activity studies on methyl (4-nitro-1-imidazolyl)acetate. *J. Indian Chem. Soc.* **2022**, *99*, 100438. [CrossRef]
41. Rincón, L.; Torres, F.J.; Almeida, R. Is the Pauli exclusion principle the origin of electron localisation? *Mol. Phys.* **2018**, *116*, 578–587. [CrossRef]
42. Burdett, J.K.; McCormick, T.A. Electron localization in molecules and solids: The meaning of ELF. *J. Phys. Chem. A* **1998**, *102*, 6366–6372. [CrossRef]
43. Nalewajski, R.F.; Köster, A.M.; Escalante, S. Electron localization function as information measure. *J. Phys. Chem. A* **2005**, *109*, 10038–10043. [CrossRef] [PubMed]
44. Weinhold, F.; Landis, C.R.; Glendening, E.D. What is NBO analysis and how is it useful? *Int. Rev. Phys. Chem.* **2016**, *35*, 399–440. [CrossRef]
45. Karthikeyan, S.; Sedlak, R.; Hobza, P. On the nature of stabilization in weak, medium, and strong charge-transfer complexes: CCSD(T)/CBS and SAPT calculations. *J. Phys. Chem. A* **2011**, *115*, 9422–9428. [CrossRef] [PubMed]
46. Weinhold, F.; Landis, C.R. Natural bond orbitals and extensions of localized bonding concepts. *Chem. Educ. Res. Pract.* **2001**, *2*, 91–104. [CrossRef]
47. Reed, A.E.; Weinstock, R.B.; Weinhold, F. Natural population analysis. *J. Chem. Phys.* **1985**, *83*, 735–746. [CrossRef]
48. Cho, M.; Sylvetsky, N.; Eshafi, S.; Santra, G.; Efremenko, I.; Martin, J.M.L. The atomic partial charges arboretum: Trying to see the forest for the trees. *ChemPhysChem* **2020**, *21*, 688–696. [CrossRef] [PubMed]
49. Yerushalmi, R.; Scherz, A.; Baldridge, K.K. Direct experimental evaluation of charge scheme performance by a molecular charge-meter. *J. Am. Chem. Soc.* **2004**, *126*, 5897–5905. [CrossRef] [PubMed]
50. Fainman, Y.; Ma, J.; Lee, S.H. Non-linear optical materials and applications. *Mater. Sci. Rep.* **1993**, *9*, 53–139. [CrossRef]
51. Kim, T.-D.; Lee, K.-S. D-π-A conjugated molecules for optoelectronic applications. *Macromol. Rapid Commun.* **2015**, *36*, 943–958. [CrossRef] [PubMed]
52. Evecen, M.; Ersanlı, C.C.; Doğan, O.E.; Bozkurt, I.; Agar, E. Synthesis and analysis (thermodynamic, electronic, NLO, FMO, NBO, MEP, IR, UV, NMR properties, Hirshfeld surface analysis and molecular docking) of the new Schiff base molecule: (Z)-4-bromo-2-(((2,4-dimethoxyphenylimino)methyl)-5-fluorophenol. *J. Mol. Struct.* **2025**, *1329*, 141454. [CrossRef]
53. Dede, B.; Avcı, D.; Bahçeli, S. Study on the 4-ethoxy-2-methyl-5-(4-morpholinyl)-3(2H)-pyridazinone using FT-IR, 1H and 13C NMR, UV-vis spectroscopy, and DFT/HSEH1PBE method. *Can. J. Phys.* **2018**, *96*, 1042–1052. [CrossRef]
54. Silverstein, R.M.; Bassler, G.C. Spectrometric identification of organic compounds. *J. Chem. Educ.* **1962**, *39*, 546. [CrossRef]
55. Van Bramer, S.E.; Bastin, L.D. Spectroscopy data for undergraduate teaching. *J. Chem. Educ.* **2023**, *100*, 3897–3902. [CrossRef]
56. Ali, A.; Din, Z.U.; Ibrahim, M.; Ashfaq, M.; Muhammad, S.; Gull, D.; Tahir, M.N.; Rodrigues-Filho, E.; Al-Sehemi, A.G.; Suleman, M. Acid catalyzed one-pot approach towards the synthesis of curcuminoid systems: Unsymmetrical diarylidene cycloalkanones, exploration of their single crystals, optical and nonlinear optical properties. *RSC Adv.* **2023**, *13*, 4476–4494. [CrossRef] [PubMed]
57. Ali, A.; Ashfaq, M.; Din, Z.U.; Ibrahim, M.; Khalid, M.; Assiri, M.A.; Riaz, A.; Tahir, M.N.; Rodrigues-Filho, E.; Imran, M.; et al. Synthesis, structural, and intriguing electronic properties of symmetrical bis-aryl-α,β-unsaturated ketone derivatives. *ACS Omega* **2022**, *8*, 39294–39309. [CrossRef] [PubMed]
58. Ali, A.; Din, Z.U.; Khalid, M.; Tahir, M.N.; Rodrigues-Filho, E.; Ali, B.; Asim, S.; Muhammad, S. Crystal and quantum chemical exploration of the potent monocarbonyl curcuminoids to unveil their structural and intriguing electronic properties. *ChemistrySelect* **2020**, *5*, 3735. [CrossRef]
59. Khalid, M.; Ali, A.; Adeel, M.; Din, Z.U.; Tahir, M.N.; Rodrigues-Filho, E.; Iqbal, J.; Khan, M.U. Facile preparation, characterization, sc-xrd and dft/dtdft study of diversely functionalized unsymmetrical bis-aryl-α,β-unsaturated ketone. *J. Mol. Struc.* **2020**, *1206*, 127755. [CrossRef]
60. Ali, A.; Khalid, M.; Din, Z.U.; Asif, H.M.; Imran, M.; Tahir, M.N.; Ashfaq, M.; Rodrigues-Filho, E. Exploration of structural, electronic and third order nonlinear optical properties of crystalline chalcone systems: Monoarylidene and unsymmetrical diarylidene cycloalkanones. *J. Mol. Struc.* **2021**, *1241*, 130685. [CrossRef]
61. Baldenebro-López, J.; Castorena-González, J.; Flores-Holguín, N.; Almaral-Sánchez, J.; Glossman-Mitnik, D. Density functional theory (DFT) study of triphenylamine-based dyes for their use as sensitizers in molecular photovoltaics. *Int. J. Mol. Sci.* **2012**, *13*, 4418–4432. [CrossRef] [PubMed]
62. Lu, T. Multiwfn: A Multifunctional Wave Function Analyzer. *J. Comput. Chem.* **2012**, *33*, 580–592.
63. O'Boyle, N.M.; Tenderholt, A.L.; Langner, K.M. cclib: A library for package-independent computational chemistry algorithms. *J. Comput. Chem.* **2008**, *29*, 839–845. [CrossRef] [PubMed]
64. Morris, G.M.; Huey, R.; Lindstrom, W.; Sanner, M.F.; Belew, R.K.; Goodsell, D.S.; Olson, A.J. AutoDock4 and AutoDockTools4: Automated docking with selective receptor flexibility. *J. Comput. Chem.* **2009**, *30*, 2785–2791. [CrossRef] [PubMed]

65. Laskowski, R.A.; Swindells, M.B. LigPlot: Multiple ligand-protein interaction diagrams for drug discovery. *J. Chem. Inf. Model.* **2011**, *51*, 2778–2786. [CrossRef] [PubMed]
66. DeLano, W.L. PyMOL: An open-source molecular graphics tool. *CCP4 Newsl. Protein Crystallogr.* **2002**, *40*, 82–92.
67. Abraham, M.J.; Murtola, T.; Schulz, R.; Páll, S.; Smith, J.C.; Hess, B.; Lindahl, E. GROMACS: High performance molecular simulations through multi-level parallelism from laptops to supercomputers. *SoftwareX* **2015**, *1*, 19–25. [CrossRef]
68. Jorgensen, W.L.; Chandrasekhar, J.; Madura, J.D.; Impey, R.W.; Klein, M.L. Comparison of simple potential functions for simulating liquid water. *J. Chem. Phys.* **1983**, *79*, 926–935. [CrossRef]
69. Wang, J.; Wolf, R.M.; Caldwell, J.W.; Kollman, P.A.; Case, D.A. Development and testing of a general amber force field. *J. Comput. Chem.* **2004**, *25*, 1157–1174. [CrossRef] [PubMed]
70. Maier, J.A.; Martinez, C.; Kasavajhala, K.; Wickstrom, L.; Hauser, K.E.; Simmerling, C. ff14SB: Improving the accuracy of protein side chain and backbone parameters from ff99SB. *J. Chem. Theory Comput.* **2015**, *11*, 3696–3713. [CrossRef] [PubMed]
71. Valdés-Tresanco, M.S.; Valdés-Tresanco, M.E.; Valiente, P.A.; Moreno, E. gmx_MMPBSA: A new tool to perform end-state free energy calculations with GROMACS. *J. Chem. Theory Comput.* **2021**, *17*, 6281–6291. [CrossRef] [PubMed]
72. Miller, B.R., III; McGee, T.D., Jr.; Swails, J.M.; Homeyer, N.; Gohlke, H.; Roitberg, A.E. MMPBSA.py: An efficient program for end-state free energy calculations. *J. Chem. Theory Comput.* **2012**, *8*, 3314–3321. [CrossRef] [PubMed]


**Disclaimer/Publisher's Note:** The statements, opinions and data contained in all publications are solely those of the individual author(s) and contributor(s) and not of MDPI and/or the editor(s). MDPI and/or the editor(s) disclaim responsibility for any injury to people or property resulting from any ideas, methods, instructions or products referred to in the content.